JACS
JOURNAL OF THE AMERICAN CHEMICAL SOCIETY
pubs.acs.org/JACS
Article

Tuning of Trifunctional NiCu Bimetallic Nanoparticles Confined in a Porous Carbon Network with Surface Composition and Local Structural Distortions for the Electrocatalytic Oxygen Reduction, Oxygen and Hydrogen Evolution Reactions

Md Ariful Ahsan, Alain R. Puente Santiago,* Yu Hong, Ning Zhang, Manuel Cano, Enrique Rodriguez-Castellon, Luis Echegoyen,* Sreeprasad T. Sreenivasan,* and Juan C. Noveron*

Cite This: J. Am. Chem. Soc. 2020, 142, 14688−14701

Read Online

ACCESS | Metrics & More | Article Recommendations | Supporting Information

ABSTRACT: The rational design of multifunctional catalysts that use non-noble metals to facilitate the interconversion between H_2, O_2, and H_2O is an intense area of investigation. Bimetallic nanosystems with highly tunable electronic, structural, and catalytic properties that depend on their composition, structure, and size have attracted considerable attention. Herein, we report the synthesis of bimetallic nickel−copper (NiCu) alloy nanoparticles confined in a sp^2 carbon framework that exhibits trifunctional catalytic properties toward hydrogen evolution (HER), oxygen reduction (ORR), and oxygen evolution (OER) reactions. The electrocatalytic functions of the NiCu nanoalloys were experimentally and theoretically correlated with the composition-dependent local structural distortion of the bimetallic lattice at the nanoparticle surfaces. Our study demonstrated a downshift of the d-band of the catalysts that adjusts the binding energies of the intermediate catalytic species. XPS analysis revealed that the binding energy for Ni $2p_{3/2}$ band of the $Ni_{0.25}Cu_{0.75}/C$ nanoparticles was shifted ∼3 times compared to other bimetallic systems, and this was correlated to the high electrocatalytic activity observed. Interestingly, the bimetallic $Ni_{0.25}Cu_{0.75}/C$ catalyst surpassed the OER performance of RuO_2 benchmark catalyst exhibiting a small onset potential of 1.44 V vs RHE and an overpotential of 400 mV at 10 mA·cm^{-2} as well as the electrochemical long-term stability of commercial RuO_2 and Pt catalysts and kept at least 90% of the initial current applied after 20 000 s for the OER/ORR/HER reactions. This study reveals significant insight about the structure−function relationship for non-noble bimetallic nanostructures with multifunctional electrocatalytic properties.

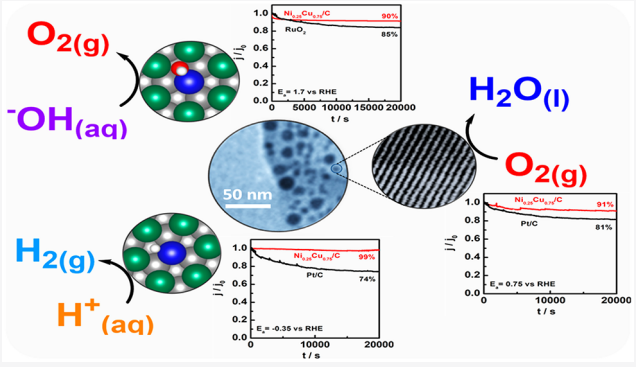

1. INTRODUCTION

The development of sustainable-energy materials and green nanotechnologies to fabricate fuel cells, metal-air batteries, and water-splitting systems has become a promising way to solve the increasing energy demands as well as the environmental-related issues of the modern society.[1−5] Among the possible renewable energy technologies, the hydrogen evolution reaction (HER), oxygen evolution reaction (OER) and oxygen reduction reaction (ORR) are leading the storage and energy conversion processes owing to their potential to create energy with zero emission. To efficiently carry out those reactions, a stable and electrochemically highly active material is critical. In this direction, noble metal catalysts, for instance, Pt-based nanomaterials, demonstrated outstanding bifunctional performances toward HER and ORR. Similarly, Ru and Ir-based catalysts are the best OER-electrocatalysts.[6,7] Nevertheless, the very high prices, poor stability and scarcity of the conventional noble metals have markedly inhibited their large-scale integration to the commercial renewable energy technologies. Hence, the sustenance of a future based on clean energy technologies will benefit from the development of inexpensive nanomaterials with enhanced multifunctional electrocatalytic properties.

Dedicated efforts in this direction resulted in the creation of a myriad of alternative materials with bifunctional or trifunctional electrocatalytic performances, including nanocarbons,[8] metal oxides,[9] carbides/nitrides, and their composites.[10−12] Among them, the development of carbon-coated transitional metal-based nanoalloys are recently gaining

Received: June 29, 2020
Published: July 27, 2020

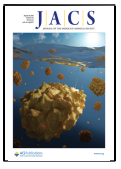

https://dx.doi.org/10.1021/jacs.0c06960
J. Am. Chem. Soc. 2020, 142, 14688−14701

increasing attention due to their fast electron transfer (ET) rates, the plethora of functionalities afforded by the carbon shell as well as the possibility to employ the volcano plots to tune their properties. Especially, the presence of multiple metals mixed at the nano level also leads to a promising strategy to improve electrocatalytic performance toward many catalytic reactions. It is worthwhile to investigate the structure-catalytic function of bimetallic transition metal nanoparticles owing to the fact that their geometric and electronic surface structure can be tailored using a wide range of controlled phase compositions and morphologies.[13] Thus, the electrocatalytic rates of bimetallic nanosystems are markedly controlled by the engineering of their nanostructure morphology, composition, as well as defect density and strain, which, in turn, facilitate the control of the binding energy states of the reactants and the intermediates catalytic species at the electrochemical interfaces. Therefore, the development of non-noble bimetallic nanostructures with multifunctional catalytic properties is currently becoming a hotspot into the energy field.

Though significant progress has been achieved regarding the synthesis of bimetallic catalysts and their use as electrocatalysts with enhanced activity,[14−17] very few efforts were made to optimize their structure to derive trifunctional catalytic properties.[18,19] Especially disentangling the underlying structural parameters that govern the electrocatalytic activity,[20] which can help to further tune and optimize the catalytic properties, is rarely attempted. In this work, a facile and eco-friendly strategy to prepare NiCu bimetallic nanoparticles (NPs) with varying Ni:Cu ratios encapsulated in a hierarchically structured carbon framework is presented. The synthesis involves the capillary force assisted spontaneous adsorption of the metal precursors into the facial tissue and the subsequent simultaneous thermal reduction and carbonization. The resulting nanoalloys displayed an efficient trifunctional catalytic activity toward HER/OER/ORR. Though all bimetallic catalysts demonstrated superior catalytic activity compared to their monometallic counterparts, the ultimate catalytical efficacy intimately depended on the composition (ratio between Ni and Cu) of the alloys. For example, the $Ni_{0.25}Cu_{0.75}$/C electrocatalyst surpassed the electrocatalytic performances of its counterparts as well as exhibited better electrocatalytic performances than commercial RuO_2 and Pt. To the best of our knowledge, this is the first report of the structural and electronic properties of non-noble NiCu nanoparticles together with their trifunctional electrocatalytic properties, which were finely controlled by varying the alloy composition. Density functional theory (DFT) calculations were carried out to validate our experimental results, as well as elucidate the underlying catalytic mechanisms of NiCu bimetallic nanoparticles (NPs) with various compositions. Finally, the DFT-calculated binding energy values were used as an optimal descriptor of the trifunctional catalytic activity, and simulation results showed that 3-fold hollow sites containing one Ni atom and two Cu atoms are the active sites for the trifunctional catalytic activity of the NiCu nanoparticles.

2. EXPERIMENTAL SECTION

2.1. Materials. All of the chemicals were used as received without any further purification. Commercial tissue paper was obtained from a local store at El Paso, Texas, USA. Copper nitrate ($Cu(NO_3)_2\cdot 2.5H_2O$), nickel nitrate ($Ni(NO_3)_2\cdot 6H_2O$), methanol, Nafion solution, sulfuric acid, sodium hydroxide, and Pt/C (20%) were purchased from Aldrich, Fisher Scientific and Sigma-Aldrich. Deionized (DI) water was obtained from the Milli-Q instrument (Millipore Corporation).

2.2. Synthesis of the Electrocatalysts. 1.5 g of $Cu(NO_3)_2\cdot 2.5H_2O$ and 1.5 g of $Ni(NO_3)_2\cdot 6H_2O$ were added into a 100 mL beaker and dissolved in 10 mL of DI water. Afterward, 3.0 g of tissue paper were dipped into the salt solution and the mixture was bath sonicated so that all the metal ions (Cu^{2+} and Ni^{2+}) were adsorbed on the surface of the tissue paper. The tissue paper was then heated to 100 °C to remove all the water. Subsequently, the tissue papers were carbonized in a tube furnace at 700 °C. High purity argon gas was passed through the tube furnace to remove air for at least 1 h prior to the carbonization process. The heating rate of the carbonization was set as 5 °C min^{-1}. The process was carried out in a high-purity argon atmosphere. The sample was carbonized for 3 h in a quartz boat. The carbonized product was taken out once the temperature reached room temperature and the product was then dispersed in a 1.0 M sulfuric acid solution with the assistance of ultrasonication to remove any unstable metallic substances.[21] The etching process was performed for 24 h. The product was collected by centrifugation and washed for several times using DI water. The obtained product was then brought to neutral pH and vacuum-dried at 70 °C for 12 h. The product was denoted as $Ni_{0.50}Cu_{0.50}$/C. Afterward, the product was put into a glass vial for further use. Two other bimetallic electrocatalysts were also prepared, namely, $Ni_{0.25}Cu_{0.75}$/C and $Ni_{0.75}Cu_{0.25}$/C by varying the wt % of the copper and nickel salts. As controls, Cu/C and Ni/C monometallic electrocatalysts were synthesized following the same procedure with only copper or nickel salt used in the synthesis process.

2.3. Materials Characterization. X-ray diffraction (XRD) experiments were performed on a Bruker D8 Discover X-ray Diffractometer. The elemental analysis and color mapping were performed using Energy dispersive spectroscopy (EDS) equipped with the SEM instrument (model: Hitachi S-4800). Transmission electron microscopic analysis was carried out on a Hitachi H-7650 microscope to further investigate the morphology and microstructure of the electrocatalysts. Scanning transmission electron microscopic (STEM) analysis was performed on a JEOL ARM200 equipped with a JEOL windowless EDS detector spectrometer for spectral mapping and imaging. The chemical valence and surface elements of the electrocatalysts were detected using X-ray photoelectron spectroscopy (XPS) on a a PHI VersaProbe II Scanning XPS Microprobe with scanning monochromatic X-ray Al Kα radiation as the excitation source (200 μm area analyzed, 52.8 W, 15 kV, 1486.6 eV), and a charge neutralizer. Thermal gravimetric analysis (TGA) was performed under a continuous nitrogen flow and at a heating rate of 10 °C/min on a Mettler Toledo thermogravimetric apparatus. Raman spectra of the electrocatalysts were collected using a DXR Smart Raman instrument. Brunauer−Emmett−Teller surface area (BET) and pore volume experiments were carried out using a Micromeritics Surface Area and Porosity Analyzer (ASAP-2020).

2.4. Electrochemical Measurements. Measurements of HER, OER, and ORR activity of the as-prepared electrocatalysts were performed with a traditional three-electrode system (CHI-640). The working, counter, and reference electrodes were glassy carbon, a graphitic rod and Ag/AgCl (KCl saturated) electrodes, respectively. 1.0 mg of electrocatalyst was mixed with 1.0 mL of methanol and bath sonicated for 30 min to make the catalyst ink. Then the catalyst ink was drop casted onto the working electrode and allowed to dry in air prior to use in the electrochemical reactions. All electrochemical HER experiments were performed in 0.5 M H_2SO_4 solution in a nitrogen saturated solution at a scan rate of 2 mV/s and all electrochemical OER and ORR experiments were performed in 0.5 M NaOH solution in an oxygen saturated solution at a scan rate of 2 mV/s. The following equation was used to calibrate the experimental potentials.[22]

$$E_{RHE} = E_{Ag/AgCl} + 0.197 + 0.059\ pH \quad (1)$$

The Tafel slope is a key parameter to describe the electrocatalytic performance and kinetics of a reaction and it can be expressed by the following equation.[22]

https://dx.doi.org/10.1021/jacs.0c06960
J. Am. Chem. Soc. 2020, 142, 14688−14701

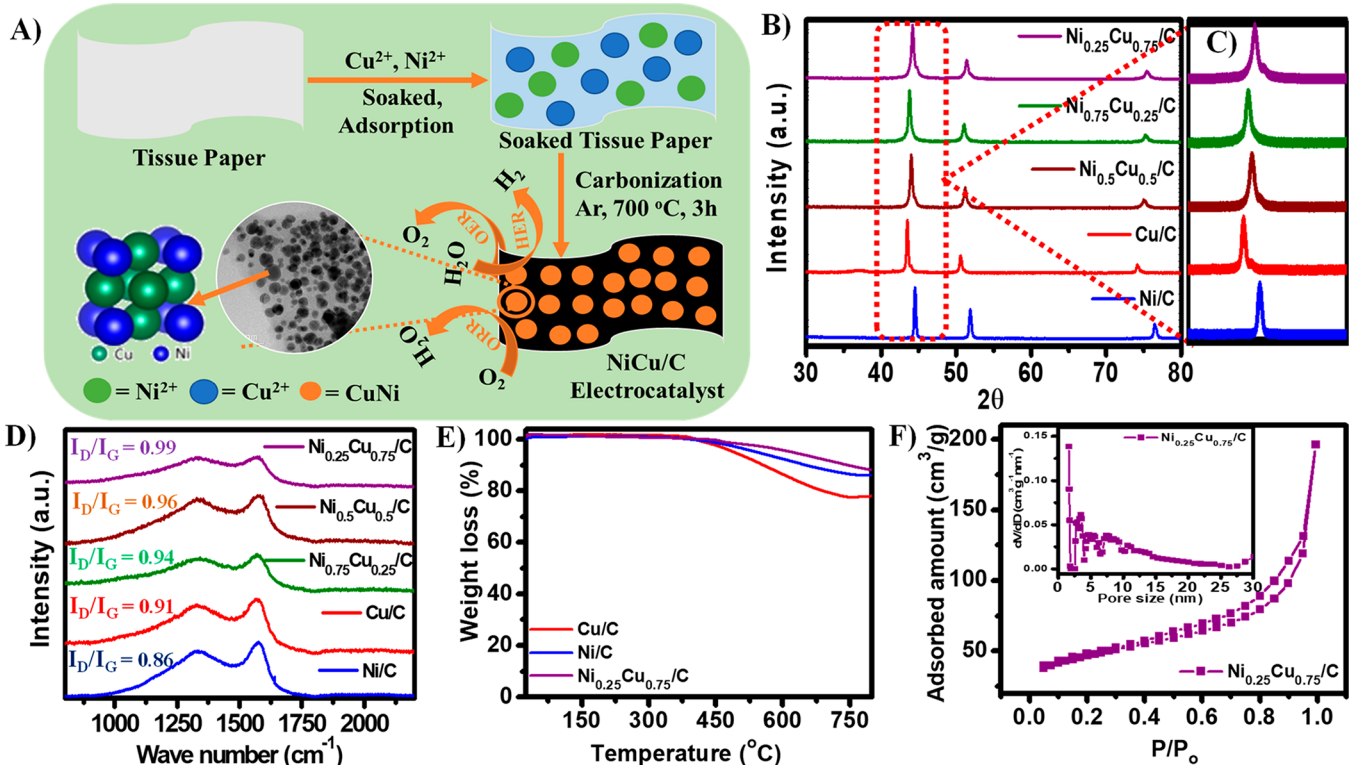

Figure 1. (A) Schematic representation of the synthesis of NiCu/C electrocatalysts. (B,C) XRD analysis of the Ni/C, Cu/C, and NiCu/C bimetallic electrocatalysts. (D) Raman spectra of the as-synthesized electrocatalysts. (E) TGA analysis of Ni/C, Cu/C, and $Ni_{0.25}Cu_{0.75}$/C electrocatalysts. (F) N_2 adsorption−desorption isotherm of the $Ni_{0.25}Cu_{0.75}$/C electrocatalyst (corresponding BJH pore size distribution).

$$\eta = a + \frac{2.3RT}{\alpha nF}\log j \tag{2}$$

where j, a, F and η are the current density, transfer coefficient, Faraday constant and overpotential, respectively; n is the number of electrons involved in the reaction, and the slope is given by $b = \frac{2.3RT}{\alpha nF}$.

The electrochemically active surface area (ECSA) of the electrocatalysts was estimated by evaluating the cyclic voltammetry (CV) measurements and the electrochemical double-layer capacitance that was tested from 0 to 0.30 V (vs RHE) in a N_2-saturated 0.5 M H_2SO_4 solution for the HER process or measurements were made between 1.0 and 1.30 V (vs RHE) in an O_2-saturated 0.5 M NaOH solution at different scan rates (5, 20, 50, 100, 150, and 200 mV/s) for the OER and ORR processes. The difference between the anodic and cathodic current (at 0.15 V vs RHE for HER or at 1.15 V vs RHE for OER and ORR) were plotted against the scan rate to obtain a linear relationship and the slopes correspond to the electrochemical double-layer capacitance (C_{dl}). The ECSA was then estimated by using the following equation.[23]

$$\text{ECSA} = \frac{C_{dl}}{C_s} \tag{3}$$

where C_s is the specific capacitance of the electrocatalysts, reported to be 0.035 and 0.04 mF·cm^{-2} in acidic and alkaline solution for the Ni-based electrocatalysts.[22,23]

The roughness factors (RF) were calculated using the following equation.

$$\text{RF} = (\text{ECSA})/(\text{geometric area of the electrode}) \tag{4}$$

A glassy carbon disc of 5 mm in diameter (Pine Instruments Company) was used as the working electrode for the rotating disc electrode (RDE) measurements. All electrochemical experiments were performed employing a potential range from 0.00 to −0.75 V vs Ag/AgCl at a scan rate of 10 mV/s. All potentials were referenced to the RHE. The kinetic parameters were estimated by applying the Koutecky−Levich (K−L) equations.[21]

$$\frac{1}{J} = \frac{1}{J_L} + \frac{1}{J_K} = \frac{1}{B\omega^{1/2}} + \frac{1}{J_K} \tag{5}$$

$$B = 0.20nFC_0D_0^{2/3}\nu^{-1/6} \tag{6}$$

$$J_K = nFkC_0 \tag{7}$$

where J is the measured current density, J_K and J_L are the kinetic and diffusion limiting current densities, respectively, ω is the electrode rotation rate, n is the overall number of electrons transferred for the oxygen reduction, F is the Faraday constant, C_0 is the bulk concentration of O_2 dissolved in the electrolyte (1.03×10^{-3} mol·L^{-1} for 0.5 M KOH), D_0 is the diffusion coefficient of O_2 (1.63×10^{-5} cm^2·s^{-1} for 0.5 M NaOH), ν is the kinematic viscosity of the electrolyte (0.01 cm^2·s^{-1} for 0.5 M NaOH), and k is the electron transfer rate constant during ORR. B* is a constant (2.76×10^{-2} A·cm^{-2}·rpm$^{-1/2}$) for all the performed experiments.

3. RESULTS AND DISCUSSION

3.1. Structural Characterization of Ni, Cu, and Bimetallic NiCu Nanostructures. Synthesis of the NiCu@C electrocatalysts was achieved via a two-steps process involving the adsorption of the corresponding metal ions into cellulose-based paper towel followed by a high-temperature carbonization, Figure 1A. First, the highly porous structure of the tissue paper that is primarily composed of lignin and cellulose was leveraged to spontaneously adsorb the corresponding metal ions (Cu^{2+} and Ni^{2+}) aided by capillary force. During the carbonization step, the tissue paper serves as the carbon source and the metal ions serve as a metal precursor to form the final carbon encapsulated structure. Here, the tissue paper retains the templated porous structure during the

https://dx.doi.org/10.1021/jacs.0c06960
J. Am. Chem. Soc. 2020, 142, 14688−14701

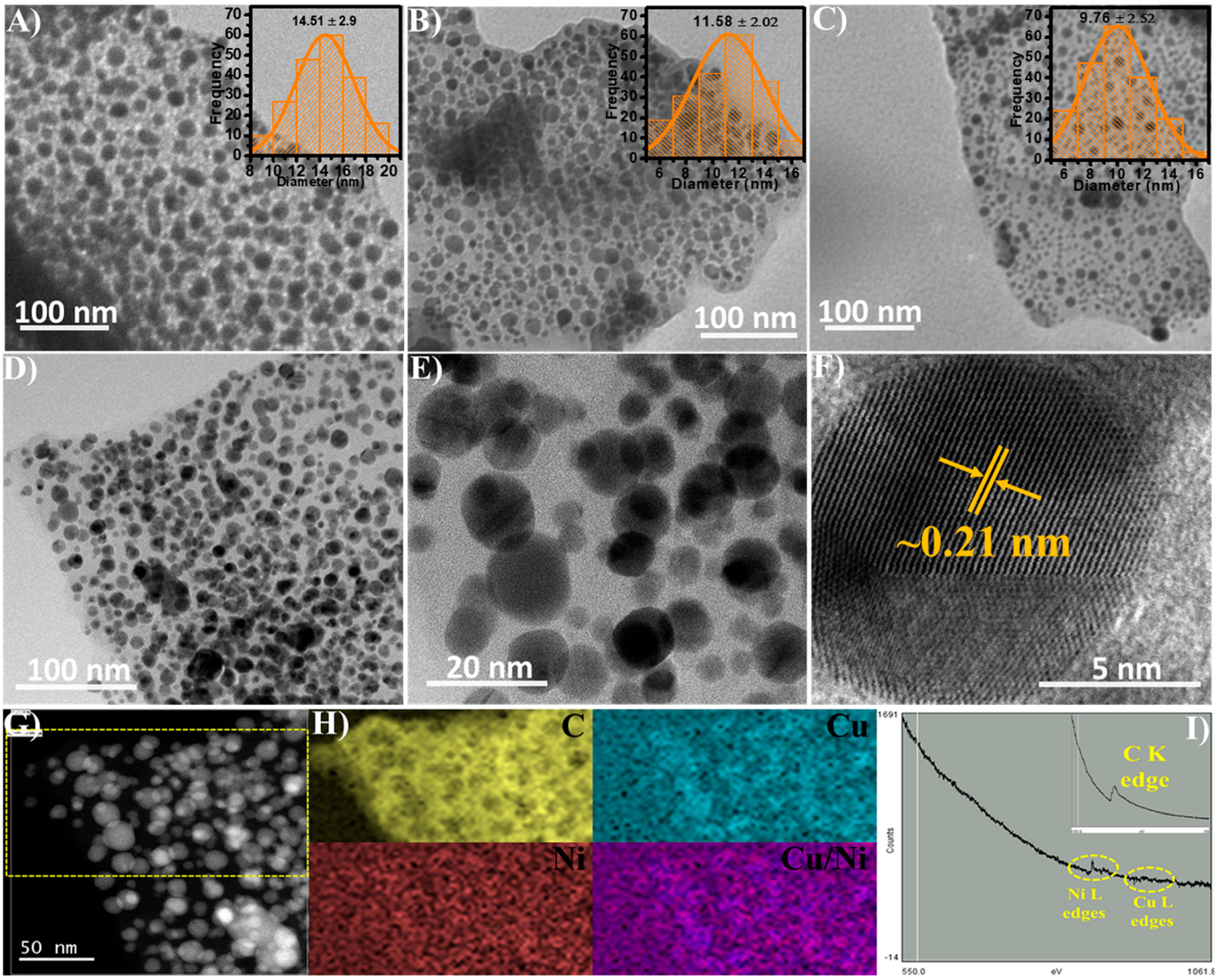

Figure 2. (A–C) TEM images of the $Ni_{0.5}Cu_{0.5}/C$, $Ni_{0.75}Cu_{0.25}/C$, and $Ni_{0.25}Cu_{0.75}/C$ electrocatalysts. (D–F) STEM images of the $Ni_{0.25}Cu_{0.75}/C$ electrocatalyst at different magnifications. (G–I) high-angle annular dark field (HAADF)-STEM image, elemental mapping images, and EELS spectra of the $Ni_{0.25}Cu_{0.75}/C$ electrocatalyst, respectively.

carbonization under inert atmosphere and gets transformed to porous carbon matrix. Simultaneously, the metal ions get reduced to NiCu nanoparticles, assisted by the in situ generated oxidative–reductive conditions during the carbothermal method. Finally, the product was treated with H_2SO_4 to remove unstable metal species formed during the reaction. Thus, through a simultaneous templated carbonization and reduction, a nanocomposite composed of uniformly dispersed and surface-clean NiCu nanoparticles encapsulated in hierarchically porous carbon was generated. The crystalline phase and structure of the as-synthesized electrocatalysts were first characterized by XRD (Figure 1B,C). The XRD had three characteristic peaks in both Cu/C and Ni/C electrocatalysts. These sharp characteristic peaks at nearly 43.4°, 50.6°, and 74.1°; and 44.5°, 51.2°, and 76.3° can be well indexed to the (111), (200), and (220) crystal planes of the face-entered cubic (FCC) Cu (JCPDS no. 04-0836) and Ni nanoparticles (JCPDS no. 04-0850), respectively.[13,24] The XRD analysis of the NiCu/C bimetallic nanoparticles also showed a similar diffraction pattern with a slight shift compared to the Cu and Ni nanoparticles. The features can be indexed to the (111), (200), and (220) crystal planes of the FCC NiCu bimetallic alloys matching with the previously reported NiCu alloys.[13,24] Further, leveraging Bragg's law and crystal geometry equation of the FCC crystals, we analyzed the structural change and lattice strain during the alloy formation (Table S1). The results indicated that the incorporation of nickel into the lattice of Cu to form the NiCu bimetallic system leads to the lattice contraction of the copper crystal structure and the highest lattice contraction was observed in the case of $Ni_{0.25}Cu_{0.75}/C$ bimetallic system. Nonetheless, the diffraction spectrum did not demonstrate any new peaks, pointing to the high purity of the as-synthesized electrocatalysts.

Compared to the characteristic high intensity peaks of the metallic Cu, Ni, or bimetallic NiCu system, the diffraction peaks of the carbon are hardly visible. However, the existence of the porous carbon matrix was verified using the Raman spectroscopy. The Raman spectra were obtained for the as-synthesized electrocatalysts and are presented in Figure 1D. Two characteristic peaks at ~1350 and ~1583 cm^{-1} were observed in all the samples that correspond to the D and G bands of the porous carbon matrix, respectively.[25] Usually, the

https://dx.doi.org/10.1021/jacs.0c06960
J. Am. Chem. Soc. 2020, 142, 14688–14701

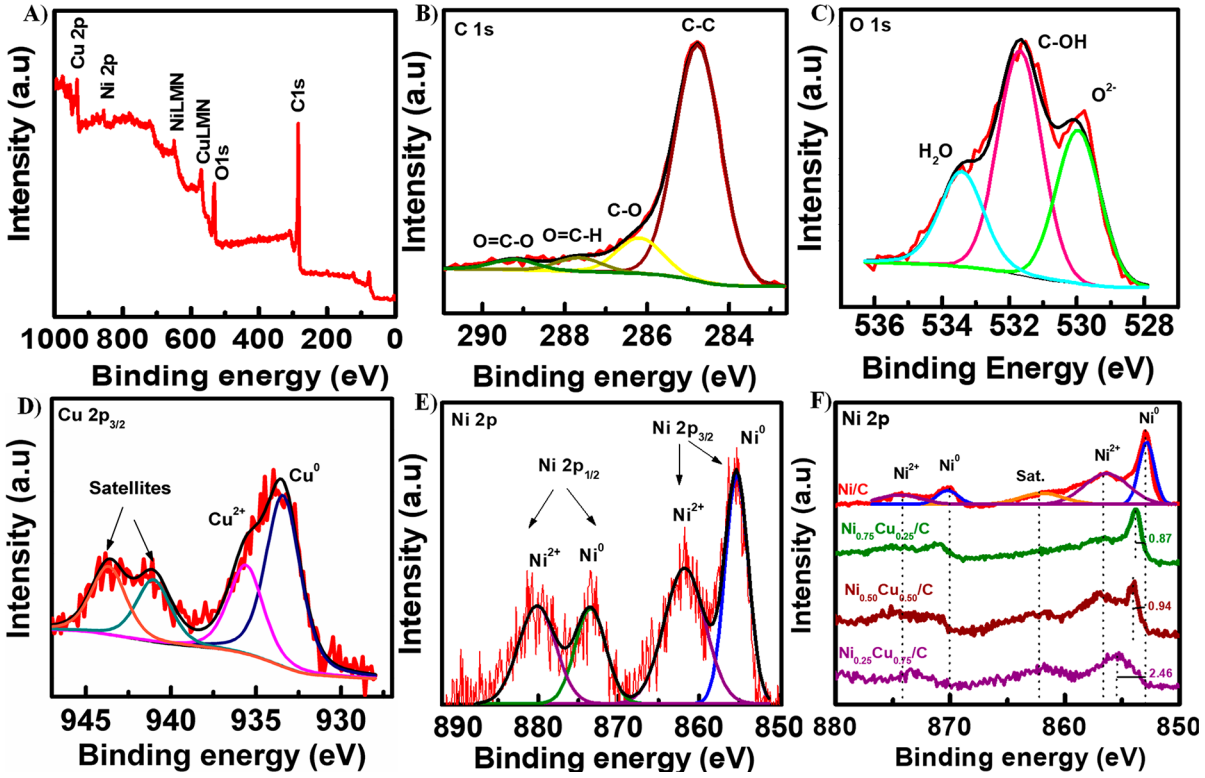

Figure 3. XPS spectra of $Ni_{0.25}Cu_{0.75}/C$ electrocatalyst: (A–E) survey spectra, C 1s, O 1s, Cu 2p, and Ni 2p, respectively; and (F) comparison of Ni 2p spectra in different electrocatalyst samples.

D band represents the disordered sp^3 carbon, whereas the G band reflects the sp^2 type graphitic carbon. Furthermore, the graphitization degree and defect density of carbon-based materials can be estimated by calculating the intensity ratio (I_D/I_G) of the D and G bands.[25] The calculated I_D/I_G values were found to be 0.86, 0.91, 0.94, 0.96, and 0.99 for the Ni/C, Cu/C, $Ni_{0.75}Cu_{0.25}/C$, $Ni_{0.50}Cu_{0.50}/C$, and $Ni_{0.25}Cu_{0.75}/C$ electrocatalysts, respectively. In the carbonization process, the tissue paper is carbonized and subsequently, the corresponding metal ions are also reduced. Moreover, the nickel can play an important catalytic role during the carbonization process and facilitate the graphitization of the porous carbon matrix.[26] Interestingly, the I_D/I_G values of the bimetallic catalysts decreased with increasing the nickel concentration, plausibly due to the promotive effect of Ni in the formation of graphitic carbon during the carbonization reaction. Furthermore, the comparatively higher I_D/I_G value of $Ni_{0.25}Cu_{0.75}/C$ electrocatalyst compared to other bimetallic systems points to the presence of higher number of defect sites especially the disordered/nongraphitic carbon in the $Ni_{0.25}Cu_{0.75}/C$. Such defect sites are known to be beneficial to enhance the HER, OER, and ORR activity.[27,28] Thermogravimetric analysis (TGA) was then performed to investigate the thermal stability of the prepared electrocatalysts and the $Ni_{0.25}Cu_{0.75}/C$ electrocatalyst displayed better thermal stability than their monometallic counterparts as seen in Figure 1E. The metal content was found to be 79.39, 87.98, and 91.75% (wt %) for Cu/C, Ni/C, and $Ni_{0.25}Cu_{0.75}/C$ electrocatalysts from the TGA analysis, respectively. Since the initial analysis indicated that $Ni_{0.25}Cu_{0.75}/C$ electrocatalyst could have superior catalytic properties, Brunauer–Emmett–Teller (BET) gas sorption measurements were conducted to investigate its surface properties. Figure 1F illustrates the nitrogen adsorption–desorption isotherm as well as the pore-size distributions (inset) of the $Ni_{0.25}Cu_{0.75}/C$ electrocatalyst. The BET surface area of $Ni_{0.25}Cu_{0.75}/C$ was found to be 157 $m^2\ g^{-1}$. The obtained isotherm was recognized as type II that is characteristic of mesoporous materials and the pore-size distribution revealed that the $Ni_{0.25}Cu_{0.75}/C$ electrocatalyst exhibit a unique mesoporous structure with an average pore size of 7.74 nm. The pore volume was found to be 0.31 $cm^3\ g^{-1}$. The mesopores in the $Ni_{0.25}Cu_{0.75}/C$ electrocatalyst can improve the electrolyte transport and the mobility of the catalytic reactant species toward the HER/OER/ORR active sites decreasing the mass transfer resistance. The higher BET surface area and pore volume of the $Ni_{0.25}Cu_{0.75}/C$ can also improve the mass transport during electrocatalytic reactions.[29]

The energy dispersive X-ray spectroscopy (EDS) analysis along with elemental mapping was performed to confirm the elemental composition of the $Ni_{0.50}Cu_{0.50}/C$, $Ni_{0.75}Cu_{0.25}/C$, and $Ni_{0.25}Cu_{0.75}/C$ electrocatalysts. As shown in Figure S3(A,B, C,D, and E,F), the EDS spectrum and elemental mapping confirmed the presence of Cu, Ni, and C in all bimetallic samples. The microstructure and morphology of the electrocatalysts was investigated by the TEM as well (Figure 2A–C and Figure S4A,B). As seen, the nanoparticles are uniformly anchored and distributed in the porous carbon matrix. Hence, the porous carbon matrix serves both as a substrate and a protecting layer for the nanoparticles and protect from further oxidation. The average particle size of the electrocatalysts were determined to be 21.04 ± 1.71, 13.86 ± 1.73, 14.51 ± 2.90, 11.58 ± 2.02, and 9.76 ± 2.52 for the Cu/C, Ni/C, $Ni_{0.5}Cu_{0.5}/C$, $Ni_{0.75}Cu_{0.25}/C$, and $Ni_{0.25}Cu_{0.75}/C$ electrocatalysts, respectively. It is well-established that the electrocatalytic reactions over a metal electrocatalyst are usually size-dependent.[29] Therefore, one can expect that the smallest nanosized

https://dx.doi.org/10.1021/jacs.0c06960
J. Am. Chem. Soc. 2020, 142, 14688–14701

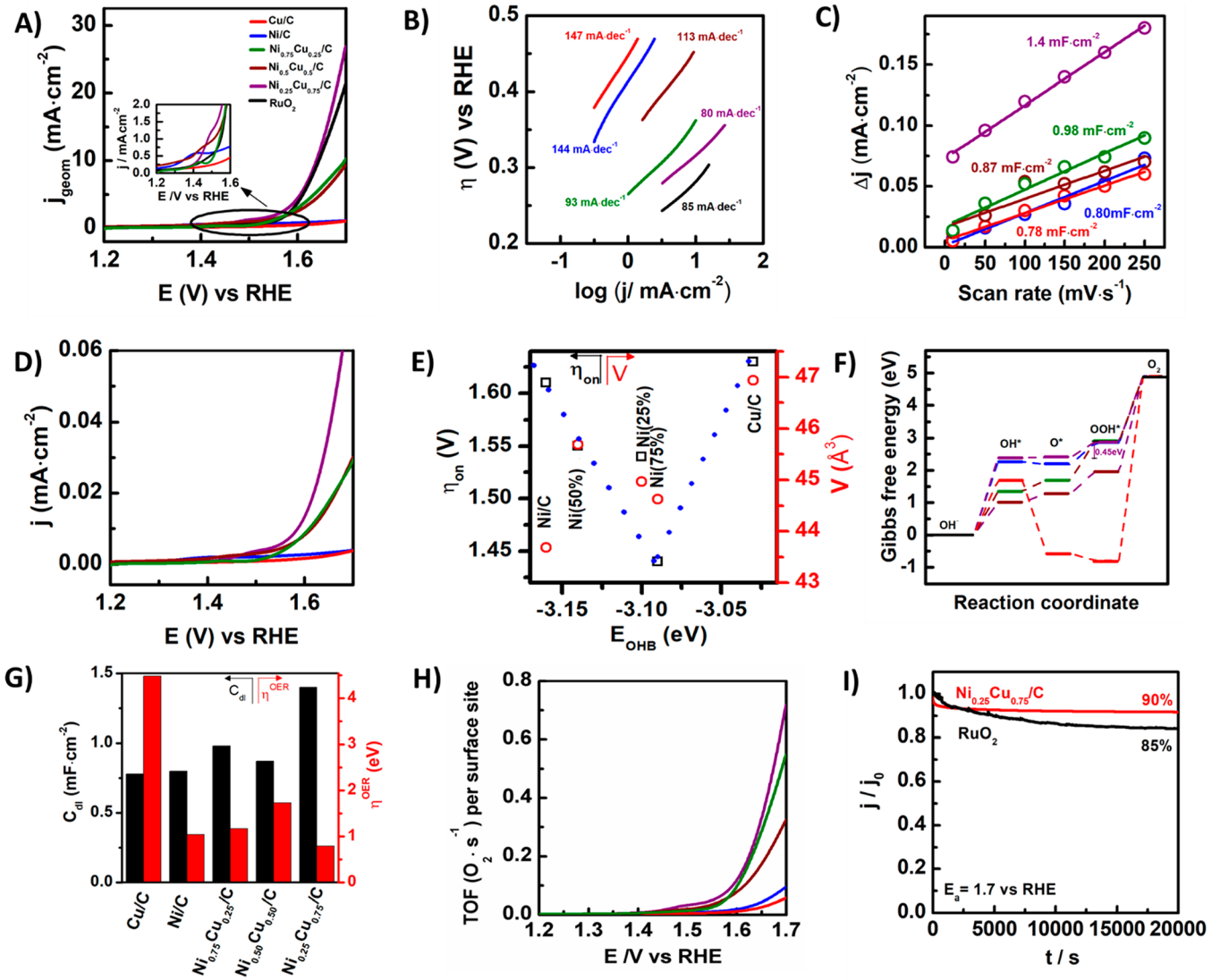

Figure 4. (A) Polarization curves of the OER process and (B) the corresponding Tafel plots for Cu/C, Ni/C, $Ni_{0.50}Cu_{0.50}$/C, $Ni_{0.25}Cu_{0.75}$/C, $Ni_{0.75}Cu_{0.25}$/C, and commercial RuO_2 in 0.5 M NaOH at 2 $mV{\cdot}s^{-1}$. (C) Plots of the difference of anodic and cathodic current densities against the scan rate for all the catalysts. (D) Polarization curves normalized by ECSA for Cu/C, Ni/C, $Ni_{0.50}Cu_{0.50}$/C, $Ni_{0.25}Cu_{0.75}$/C, and $Ni_{0.75}Cu_{0.25}$/C. (E) The corresponding onset potential and unit cell volume values for Cu/C, Ni/C, $Ni_{0.50}Cu_{0.50}$/C, $Ni_{0.25}Cu_{0.75}$/C, and $Ni_{0.75}Cu_{0.25}$/C as a function of the DFT-calculated E_{OHB}. (F) The corresponding free energy for the OER pathways for each nanoalloy. (G) The relationship between the C_{dl} and ΔG_{H^*} values for all systems. (H) The average turnover frequencies (TOF_{avg}) of the nanocatalysts displayed in (A) per surface site. (I) I–t curves for $Ni_{0.25}Cu_{0.75}$ and its comparison with commercial RuO_2 at 1.70 V vs RHE.

$Ni_{0.25}Cu_{0.75}$/C electrocatalyst among others with a narrow size distribution can offer an abundance of accessible electrocatalytic active sites, resulting in superior efficacy for electrocatalytic applications.[29]

Scanning transmission electron microscopy (STEM) was leveraged to examine the crystal structure of the NiCu bimetallic NPs, especially the $Ni_{0.25}Cu_{0.75}$/C nanohybrid system. At lower magnification, the STEM images showed a consistent result to the TEM image of the $Ni_{0.25}Cu_{0.75}$/C electrocatalyst as shown in Figure 2D,E demonstrating that the NiCu NPs are incorporated into the porous carbon structure. The bimetallic NPs are also rarely agglomerated, demonstrating a good dispersion into the porous carbon matrix. Hence it is reasonable to conclude that the framework of carbon matrix on which the nanosized NiCu NPs uniformly embedded can efficiently prevent the NPs from being excessively oxidized and agglomerating, and might facilitate the faster electron transport between the NiCu NPs and the carbon matrix, leading to efficient electrocatalytic performance. It should also be mentioned that the transition metals or their oxide phases within the carbon shells are expected to be conducive to significantly enhance the catalytic performance of the electrocatalysts that has been reported previously.[30] Hence, it is also most likely that our developed NiCu/C nanohybrid system may work following the similar mechanism due to the inherent interaction between the carbon matrix and the small-sized NiCu NPs. The STEM image also demonstrated that the NPs are highly crystalline as seen in Figure 2F, with an interplanar spacing of ~0.21 nm that corresponds to the (111) facet of the bimetallic NiCu alloy.[26] Additionally, the high-angle annular dark field (HAADF)-STEM imaging and electron energy-loss spectroscopy (EELS) was leveraged to confirm the formation of carbon-wrapped NiCu bimetallic nanoparticles at single nanoparticle levels. The HAADF-STEM image of the

https://dx.doi.org/10.1021/jacs.0c06960
J. Am. Chem. Soc. 2020, 142, 14688−14701

$Ni_{0.25}Cu_{0.75}/C$ electrocatalyst displayed the carbon-wrapped NiCu bimetallic nanoparticles (Figure 2G). The STEM-based elemental mapping of the $Ni_{0.25}Cu_{0.75}/C$ confirmed the coexistence and distribution of the C, Cu and Ni elements in the sample (Figure 2H). As seen in Figure 2I, the EELS detected three signals including C K edge (~284 eV), Ni L edge (~855 eV) and Cu L edge (~935 eV) confirming the presence of C, Ni, and Cu in the $Ni_{0.25}Cu_{0.75}/C$ electrocatalyst. In the case of 3d transition metals, the intensities of the $L_{2,3}$ white lines decrease nearly linearly with the increasing atomic number, indicating the filling of the d orbitals. As seen in Figure 2I, the metallic nickel showed the two L_3 and L_2 lines clearly in the energy-loss spectra, whereas the metallic copper did not show the L_3 and L_2 lines owing to the fully occupied d orbitals in copper.[31]

XPS measurements were used to interrogate the chemical forms of the mono- and bimetallic carbon-encapsulated metallic nanoparticles as shown in Figure 3 and Figure S5–S8. Monometallic Ni/C nanoparticles show at least two nickel species, where the Ni $2p_{3/2}$ signal can be decomposed in two contributions at and Ni $2p_{1/2}$ at 853.0 and 853.6 eV. The former is assigned to Ni^0 and the later to Ni^{2+}. While the Cu/C nanoparticles also display two contributions in the Cu $2p_{3/2}$ signal at 932.8 and 935.2 eV, assigned to Cu^0 and Cu^{2+}, respectively (Figure S5D and S6D). The assignation to Cu^0 was also supported by the Cu LMM signal (not shown). Remarkably, all the bimetallic nanoalloys underwent a positive shift of the main Ni $2p_{3/2}$ core peak indicating a change in the electronic properties of the resulting nanoalloys. The blue-shifts of the binding energies are intimately related to the d-band shifts in different bimetallic nanosystems and, in turn, with their electrocatalytic activities.[13,32] Notably, the binding energy for Ni $2p_{3/2}$ band of the $Ni_{0.25}Cu_{0.75}/C$ nanoparticles were shifted ~3 times (ΔBE) compared to other bimetallic systems (Figure 3F), suggesting a substantial change in the surface electronic properties for the $Ni_{0.25}Cu_{0.75}/C$ nanoalloys.[13] This shift could further facilitate the downshift of the d-band center and, consequently, boost the overall rates of interfacial catalytic processes. Ni and Cu contents at the nanoalloy surfaces were estimated from the integrated areas of the Ni 2p and Cu 2p regions (Table S2). It is very important to point out that the $Ni_{0.25}Cu_{0.75}/C$ nanoalloys showed the lesser number of Ni contents on the nanoparticle surfaces (~5.3%), almost two times smaller compared with the other two bimetallic nanoparticles. Taking into account the role of Ni content in enhancing the number of nanoalloy structural defects (see Raman analysis), it is reasonable to state that the $Ni_{0.25}Cu_{0.75}/C$ bimetallic nanoparticles hold the larger number of surface defect sites on their metallic frameworks. Additionally, the C 1s and O 1s spectra were also recorded to obtain in-depth information about the oxygen-containing species. The C 1s band was deconvoluted into four peaks with binding energies of oxygen-containing species. The C 1s band was deconvoluted into four peaks with binding energies of 284.8, 286.2, 287.8, and 289.3, which are attributed to C—C, C—O, O=C—H, and O=C—O bonds, respectively (Figure 3B).[29] Furthermore, the O 1s spectrum was deconvoluted into three components with binding energies of 530, 531.7, and 533.4 eV, which are associated with O^{2-}, bridging hydroxyls and physically absorbed water, respectively (Figure 3C).[33] Besides, the TGA analysis revealed that the total mass fraction of copper and nickel is about 91.75 wt % (Figure 1E) in $Ni_{0.75}Cu_{0.25}/C$ sample, which is much larger than that obtained from the XPS analysis (21.99 wt %) (Table S2). This is due to the fact that the XPS measurements are more sensitive to the surface chemical composition, which could barely detect the NiCu nanoparticles deeply embedded in the carbon matrix.

3.2. OER Activities of Ni, Cu, and Bimetallic NiCu Nanostructures. The OER properties of the Cu/C and Ni/C nanoparticles, as well as their bimetallic mixtures, were measured in 0.5 M NaOH solutions. Figure 4A displays the OER polarization curves for $Ni_{0.75}Cu_{0.25}/C$, $Ni_{0.50}Cu_{0.50}/C$, and $Ni_{0.25}Cu_{0.75}/C$ bimetallic nanocatalysts, along with Ni/C, Cu/C, and the benchmark RuO_2. The overall OER activity of the binary nanoalloys surpassed by far the performance of the individual metals indicating that the combination of Ni and Cu is generating highly active sites and boosting the catalytic rates for the generation of molecular oxygen. For example, the overpotential value to reach 10 $mA{\cdot}cm^{-2}$, which represents a suitable descriptor of the catalytic activity, is significantly lower for the bimetallic nanoparticles compared to the monometallic counterparts. Moreover, among the different nanoalloys, $Ni_{0.25}Cu_{0.75}/C$ exhibited the best OER performance, delivering a current density of 10 $mA{\cdot}cm^{-2}$ at a low overpotential of 400 mV and an onset potential of 1.44 V vs RHE, while $Ni_{0.75}Cu_{0.25}/C$ and $Ni_{0.50}Cu_{0.50}/C$ require 470 and 480 mV to achieve the same current density and exhibit onset potential values of 1.49 and 1.52 V vs RHE, respectively (Table S3). It is worth noting that the η_{10} for $Ni_{0.25}Cu_{0.75}/C$ is ~10 mV lower than that of commercial RuO_2 and comparable to other carbon-coated transition bimetallic OER catalysts (Table S7).[14,34] From the Tafel plots of different catalysts in Figure 4B, we can see that the Tafel slope of $Ni_{0.25}Cu_{0.75}/C$ is 80 $mV{\cdot}dec^{-1}$, which is the lowest value of all the samples studied including commercial RuO_2. The lower Tafel slope indicates the faster electrokinetic of the water oxidation process on the surfaces of $Ni_{0.25}Cu_{0.75}/C$ nanoparticles. Interestingly, there are substantial changes in the anodic peak potentials and intensity values of the bimetallic nanocatalysts compared to the monometallic Ni/C catalysts (Figure 4A, inset). The anodic peak of the Ni/C OER polarization curve is approximately 1.40 V, which is typically attributed to redox reactions on surface active Ni sites.[35] The area under the anodic peaks of $Ni_{0.75}Cu_{0.25}/C$, $Ni_{0.50}Cu_{0.50}/C$, and $Ni_{0.25}Cu_{0.75}/C$, which are centered at 1.38, 1.44, and 1.48 V, respectively, are very different (Figure S9). Taking into account the area under the peaks, which is mainly associated with NiOOH formation,[36] the number of accessible Ni sites for $Ni_{0.75}Cu_{0.25}/C$, $Ni_{0.50}Cu_{0.50}/C$, and $Ni_{0.25}Cu_{0.75}/C$ were estimated to be 4.58×10^{14}, 5.28×10^{14}, and 7.90×10^{14}, respectively, showing that $Ni_{0.25}Cu_{0.75}/C$ exhibits the largest number of in situ Ni active sites at the surfaces. From the XPS analyses, the wt % of Ni at the surface of the bimetallic catalysts were 9.45, 9.97, and 5.27 for $Ni_{0.75}Cu_{0.25}/C$, $Ni_{0.50}Cu_{0.50}/C$, and $Ni_{0.25}Cu_{0.75}/C$, respectively (Table S2). These results illustrate that although $Ni_{0.25}Cu_{0.75}/C$ has fewer Ni species at the surface, it has more in situ effective OER active sites. These findings can be rationalized by the fact that not all of the Ni atoms at the surface of the bimetallic nanoparticles are electrochemically active. It means that only a small percent of surface Ni atoms are capable of efficiently catalyzing the water oxidation processes. It has been reported that the OER catalytic performance of nickel (oxy)hydroxide films is substantially improved upon the addition of small quantities of iron atoms.[37] This behavior was explained on the basis of structural distortions produced through the incorporation of iron atoms

https://dx.doi.org/10.1021/jacs.0c06960
J. Am. Chem. Soc. 2020, 142, 14688–14701

into the coordination environment of Ni atoms, leading to improved overall catalytic activity. Hence, it is reasonable to think that increasing the number of Cu atoms at the bimetallic nanoparticle surfaces induces the changes in their lattice structures, which, in turn, influence both the adsorption energies of the intermediate catalytic species and the electrochemical performance of the Ni active sites. $Ni_{0.25}Cu_{0.75}/C$ also had the largest number of structural defects, which was confirmed by Raman experiments. Additionally, it was shown by XPS that the binding energy shifts on the Ni $2p_{3/2}$ band of $Ni_{0.25}Cu_{0.75}/C$ surpassed by almost a factor of 3 than those of the other two bimetallic structures. The aforementioned binding energy shift is most likely produced by more disorder in the coordination environment of the Ni atoms, which in fact markedly increase the strain energy at the interfaces of the nanodomains, thus facilitating the downshift of the d-band center as well as the lowering of the binding energies of the intermediate catalytic species[38,39] and, in turn, the activation of a larger number of Ni active sites at the nanoparticle surfaces.

The Ni-based catalysts follow three well-defined steps in the OER process:[40,41]

$$NiOOH + OH^- \leftrightarrow NiO(OH) + e^- \quad E^\circ = 1.43\ V \tag{8}$$

$$NiO(OH)_2 + 2OH^- \leftrightarrow NiOO_2 + 2H_2O + 2e^- \quad E^\circ = 1.55\ V \tag{9}$$

$$NiOO_2 + OH^- \leftrightarrow NiOOH + O_2 + e^- \tag{10}$$

Steps 8 and 9 are both reversible processes and step 10 is irreversible and usually regulates the overall OER rates. Consequently, catalytic materials speed up step 10. We believe that the enhanced catalytic activity of $Ni_{0.25}Cu_{0.75}/C$ is driven by the introduction of additional surface defects into the crystalline NiCu framework. To get in-depth information on the intrinsic activity of the electrocatalysts, the electrochemical surface areas (ECSA) and roughness factor (RF) of the monometallic and bimetallic nanoparticles were calculated from the double layer capacitance C_{dl}. The C_{dl} of $Ni_{0.25}Cu_{0.75}/C$ nanocatalysts surpassed by a factor of 2 than the values of the other bimetallic nanoparticles, reaching 1.4 $mF{\cdot}cm^{-2}$ (Figure 4C), which clearly confirmed the higher number of accessible OER active sites on these nanocatalysts. The OER polarization curves were normalized by ECSA (Figure 4D) and $Ni_{0.25}Cu_{0.75}/C$ still exhibited the best OER activity with the smallest onset potential values (1.50 V vs RHE).

Valuable insights were obtained by plotting both overpotential and unit cell volume values of all the carbon-encapsulated metallic nanoparticles as a function of the DFT-calculated OH^- adsorption energy (E_{OHB}) (Figure 4E). The superior performance of $Ni_{0.25}Cu_{0.75}/C$ perfectly matches the moderate value of E_{OHB}, which greatly favors the adsorption of the hydroxyl groups on each catalytic step since the adsorption of these anions is not too strong, nor too weak as stated by the Sabatier rule for ideal catalysts. The plot of the experimental OER onset potential values as a function of the E_{OHB} followed the typical volcano-shape trend, where the $Ni_{0.25}Cu_{0.75}/C$ is situated at the minimum of the peak, indicating superior electrocatalytic activity. These findings could be explained in terms of local structural distortions of the electrochemical interfaces of $Ni_{0.25}Cu_{0.75}/C$, which activates several Ni sites, allowing the adsorption/desorption processes of the hydroxyl anions and improving the overall OER rates. It was also observed a pronounced lattice contraction of the $Ni_{0.25}Cu_{0.75}/C$ metallic frameworks (Table S1). The lattice contraction results in additional strain effects at the interfaces which potentially favors the processes discussed above and, therefore, the catalytic efficiency of $Ni_{0.25}Cu_{0.75}/C$ nanocatalysts.[42,43] To determine whether the local structural changes at the surfaces of the bimetallic nanoparticles were beneficial to the OER reaction, the free energy diagrams were calculated by DFT (Figure 4F). According to the simulation results, $Ni_{0.25}Cu_{0.75}/C$ system exhibited the most efficient OER Gibbs free energy value of 0.79 eV, which indicated that the formation of the O*, OH*, and OOH* intermediate catalytic species were more energetically favorable on the highly distorted $Ni_{0.25}Cu_{0.75}/C$ surfaces. It implied that the surface defects of the nanoalloy material decreased the uphill energy states of each step of the OER process and enhanced the overall catalytic activity toward the water oxidation. Interestingly, the $Ni_{0.25}Cu_{0.75}/C$ exhibited a considerably lower η^{OER} value (0.79 eV) than that of the $Ni_{0.75}Cu_{0.25}/C$ (1.17 eV), $Ni_{0.50}Cu_{0.50}/C$ (1.73 eV), Cu/C (4.48 eV), and Ni/C (1.04 eV) (Figure 4G). Additionally, DFT calculations revealed that the more energetically favorable catalytic active sites on the NiCu nanoalloys were located in the 3-fold hollow sites of NiCu (111) surfaces (Figure 5). The

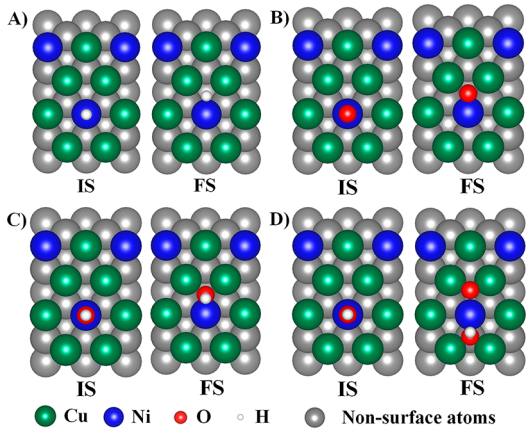

Figure 5. (A) H* adsorbed on the surface of NiCu ($Ni_{0.25}Cu_{0.75}$ is used here as an example), initial state (IS) and final state (FS). (B) O* adsorbed on the surface of NiCu. (C) OH* adsorbed on the surface of NiCu. (D) OOH* adsorbed on the surface of NiCu.

oxygen turnover frequencies (TOF) were calculated to further examine the intrinsic OER activities (Table S3). The TOF value of $Ni_{0.25}Cu_{0.75}/C$ was found to be much higher than the others, indicating their superior intrinsic activity for the OER. The current densities were normalized to TOF and then plotted against the potential to verify the theoretical results (Figure 4H), and as shown, the higher performance of $Ni_{0.25}Cu_{0.75}/C$ compared to the other nanocatalysts reinforces the observed larger OER intrinsic activity for $Ni_{0.25}Cu_{0.75}/C$ nanoalloys. It was further demonstrated by their higher mass and specific activity values (Table S3). Additionally, $Ni_{0.25}Cu_{0.75}/C$ nanoalloys showed excellent electrochemical long-term stability properties in basic media, keeping 97% of the initial current applied after 20 000 s and beating the stability of Pt/C under the same experimental conditions (Figure 4I).

3.3. HER Activities of Ni, Cu, and Bimetallic NiCu Nanostructures. The HER properties of the bimetallic nanoparticles were evaluated using a three-electrode electro-

https://dx.doi.org/10.1021/jacs.0c06960
J. Am. Chem. Soc. 2020, 142, 14688−14701

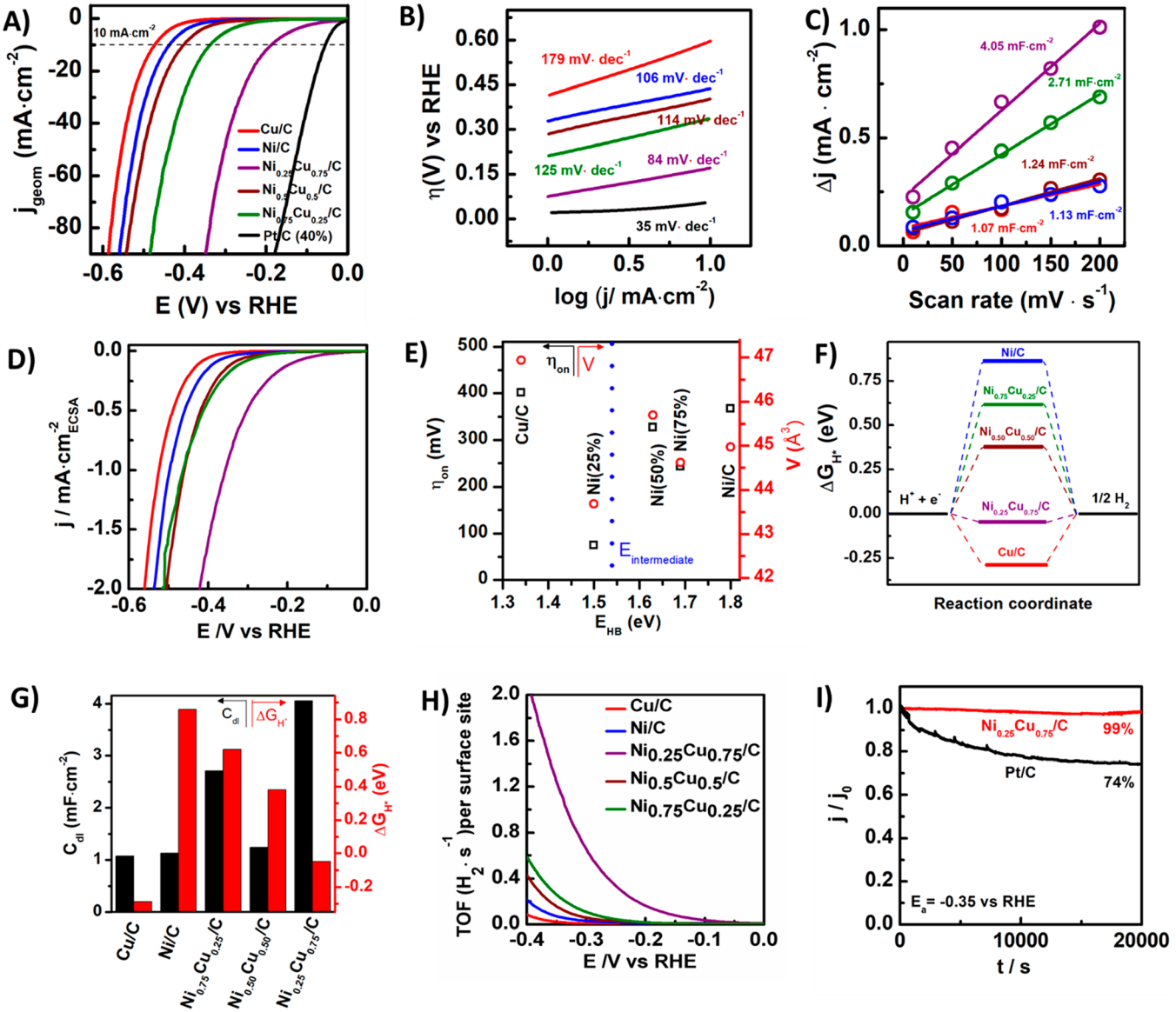

Figure 6. (A) Polarization curves of HER process and (B) the corresponding Tafel plots for Cu/C, Ni/C, $Ni_{0.50}Cu_{0.50}$/C, $Ni_{0.25}Cu_{0.75}$/C, $Ni_{0.75}Cu_{0.25}$/C, and commercial Pt/C in 0.5 M H_2SO_4 at 2 mV·s^{-1}. (C) Plots of the difference of anodic and cathodic current densities against the scan rate for all the catalysts. (D) Polarization curves normalized by ECSA for Cu/C, Ni/C, $Ni_{0.50}Cu_{0.50}$/C, $Ni_{0.25}Cu_{0.75}$/C, and $Ni_{0.75}Cu_{0.25}$/C nanocatalysts. (E) The onset potential and unit cell volume values for Cu/C, Ni/C, $Ni_{0.50}Cu_{0.50}$/C, $Ni_{0.25}Cu_{0.75}$/C, and $Ni_{0.75}Cu_{0.25}$/C as a function of the DFT-calculated E_{HB}. (F) The corresponding ΔG_{H^*} for each nanoalloy. The closer the line is to 0 indicates a better HER performance. (G) Relationship between the C_{dl} and ΔG_{H^*} values for all the electrocatalysts. (H) The average turnover frequencies (TOF_{avg}) of the nanocatalysts displayed in (A) per surface site. (I) *I*–*t* curves of $Ni_{0.25}Cu_{0.75}$ and its comparison with commercial Pt/C at −0.35 V vs RHE.

chemical system in 0.5 M H_2SO_4 (Figure 6A). All the potentials were referred to the reversible hydrogen electrode (RHE) and all the linear sweep voltammograms (LSVs) are shown with the corresponding *iR*-correction. Among all the samples, $Ni_{0.25}Cu_{0.75}$/C exhibited the highest electrocatalytic performance, delivering a very low onset potential of −75 mV vs RHE as well as an overpotential of 184 mV at a geometrical current density of 10 mA·cm^{-2}, which is lower than that of $Ni_{0.75}Cu_{0.25}$/C (334 mV), $Ni_{0.50}Cu_{0.50}$/C, (400 mV), Cu/C (471 mV) and Ni/C (437 mV). These values are comparable or even better than many other recently reported electrocatalysts (Table S8). To gain further insight on the HER kinetics, Tafel plots were fitted to the equation $\eta = a \log j + b$, where η is the overpotential, a is the slope, and j is the current density (Figure 6B). The Tafel slope for $Ni_{0.25}Cu_{0.75}$/C (84 mV·dec^{-1}) is much smaller than for both pure Ni/C (106 mV·s^{-1}) and Cu/C (179 mV·s^{-1}) and the other two nanoalloys $Ni_{0.75}Cu_{0.25}$/C (114 mV·s^{-1}) and $Ni_{0.50}Cu_{0.50}$/C (125 mV·s^{-1}), indicating that the Ni:Cu (1:3) ratio into the NiCu nanodomains markedly improves the kinetics of the HER processes through a Volmer–Heyrovsky mechanism.

To investigate the intrinsic activity of the as-synthesized electrocatalysts, the electrochemical surface area (ECSA) and RF of the electrocatalysts were calculated from the double layer capacitance (C_{dl}) values using cyclic voltammetry (CV), and the results are presented in Figure 6C and Table S6.[44] The $Ni_{0.25}Cu_{0.75}$/C electrocatalyst displayed the highest ECSA of about 115 cm^2, which is several times higher than those of the other electrocatalysts. The results obtained from both approaches demonstrate more electrocatalytically active sites

https://dx.doi.org/10.1021/jacs.0c06960
J. Am. Chem. Soc. 2020, 142, 14688−14701

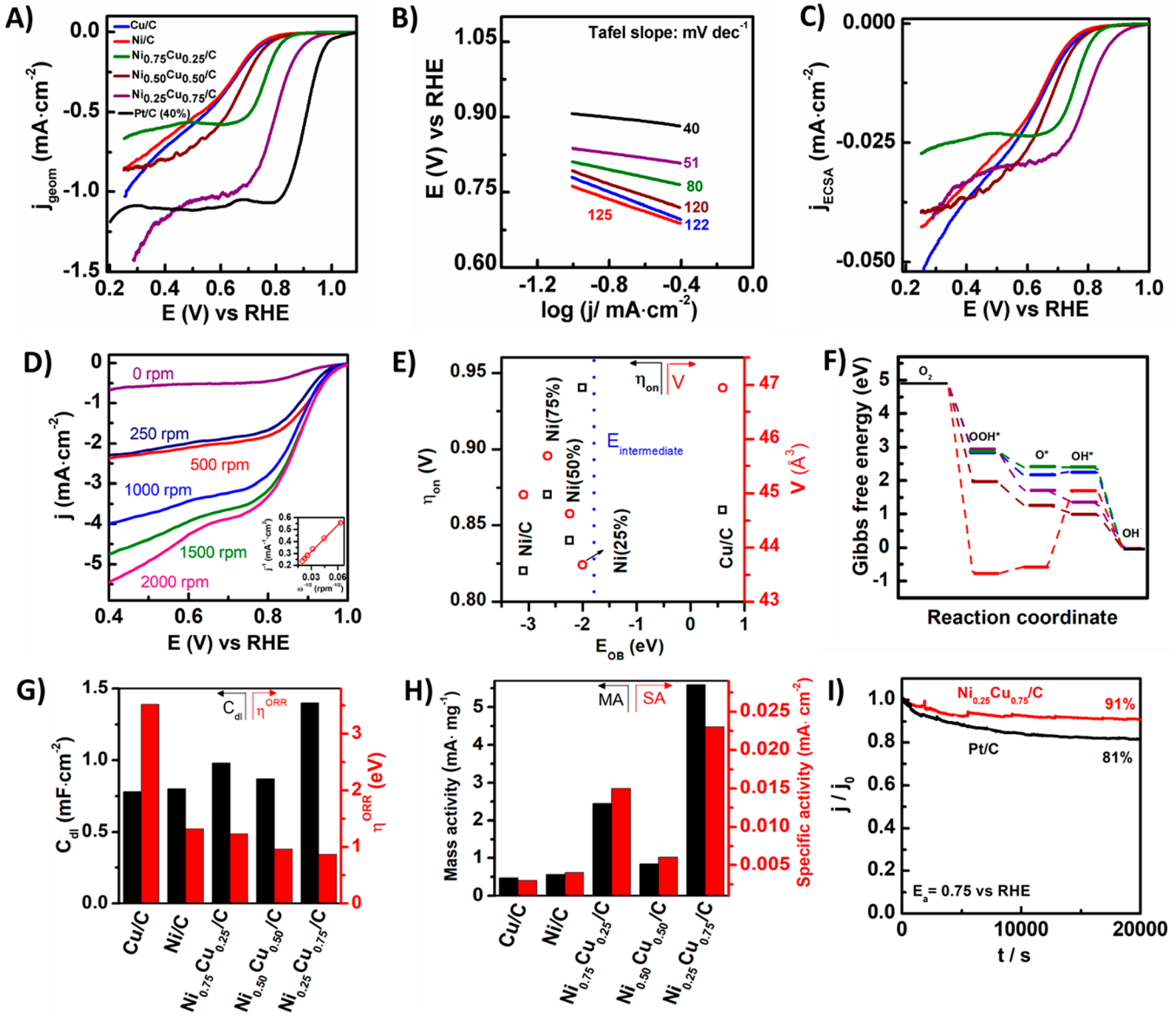

Figure 7. (A) Polarization curves of the ORR process and (B) the corresponding Tafel plots for Cu/C, Ni/C, $Ni_{0.50}Cu_{0.50}$/C, $Ni_{0.25}Cu_{0.75}$/C, $Ni_{0.75}Cu_{0.25}$/C, and commercial Pt/C in 0.5 M NaOH at 2 mV·s^{-1}. (C) Polarization curves normalized by ECSA for Cu/C, Ni/C, $Ni_{0.50}Cu_{0.50}$/C, $Ni_{0.25}Cu_{0.75}$/C, and $Ni_{0.75}Cu_{0.25}$/C. (D) Rotating disk voltammogram (RDV) curves at different rotation rates for all the samples. Inset: K−L plots. (E) ORR onset potential and unit cell volumes as a function of the DFT-calculated E_{OB}. (F) Free energies for the ORR pathways for all catalysts. (G) Relationship between C_{dl} and ΔG_{H^*} values for all electrocatalysts. (H) Mass activity (MA) and specific activity (SA) values for all the nanocatalysts. (I) I−t curves for $Ni_{0.25}Cu_{0.75}$ and its comparison with commercial Pt/C at 0.7 V vs RHE.

in $Ni_{0.25}Cu_{0.75}$/C than in the others, confirming its better electrocatalytic performance for HER process. The polarization HER curves were normalized by ECSA (Figure 6D) and $Ni_{0.25}Cu_{0.75}$/C still exhibited better HER activities with the lowest onset potential value (−0.11 V vs RHE). It is well-known that the hybridization state of different atoms in nanostructured alloys can finely tune their electrocatalytic properties. For instance, it has been demonstrated that the combination of Ni and Mo significantly improves the electrocatalytic properties for hydrogen generation.[45,46] On the other hand, it is possible to regulate the catalytic activity of bimetallic nanostructures by controlling their electronic structure as well as the strain energy and/or lattice contractions by changing their metal−metal ratios.[13,47−49] As it was explained in the OER section, the surface defects induced by an increase of Cu atoms in the crystalline framework of $Ni_{0.75}Cu_{0.25}$/C plays a significant role in the electrocatalytic activity. It is reasonable to assume that other composition-dependent effects derived from local structural distortion processes of multimetallic nanocrystal interfaces, such as the lattice dimension, the strain energy, and/or the number of energetically favorable binding sites, could be directly controlling the electronic structures of the resulting bimetallic nanocatalysts and, in turn, their HER performances.[50] The strain effects are caused when the surface atom geometries are compressed or expanded. In a bimetallic nanosystem, it can regulate both the electronic structure and the binding energy of intermediate HER catalytic species, such as H*, on the nanoalloy surfaces, which results in the deactivation or activation of the catalytically active surface sites.[51] To probe the underlying factors that govern the HER activity in our bimetallic NiCu particles, their onset potential

https://dx.doi.org/10.1021/jacs.0c06960
J. Am. Chem. Soc. 2020, 142, 14688−14701

and the unit cell volume values were plotted as a function of the DFT-calculated hydrogen binding energy (E_{HB}) (Figure 6E). The E_{HB} is an excellent descriptor of the HER catalytic activity, and it is closely linked with the position of the metal d-band center relative to the Fermi level of the nanocatalyst.[13] Interestingly, the unit cell volume values of the bimetallic nanostructures decrease together with the onset potential values, following the trend $Ni_{0.50}Cu_{0.50}/C$ > $Ni_{0.75}Cu_{0.25}/C$ > $Ni_{0.25}Cu_{0.75}/C$, which indicates that the lattice contraction of the nanoalloys is markedly improving their catalytic performance. It is well-known that when two metals with different lattice parameters are mixed to form a bimetallic system, a lattice mismatch is generated at the interface of the metal nanodomains, which leads to a lattice distortion in the crystalline framework.[50,52,53] The defective sites can create additional strain effects at the interfaces of the nanodomains which facilitate the distortion of the lattice parameters, and in turn, their pronounced lattice contraction. The lattice contraction gives rise to the downshift of the d-band center, which, in turn, decreases the adsorption energy of the reaction intermediate species boosting the catalytic efficiency of $Ni_{0.25}Cu_{0.75}/C$ toward the generation of molecular hydrogen.[54−56] The Sabatier principle predicts that interactions between reactants and intermediates and the catalyst surface must be ideally balanced to reach very high catalytic performances. In this sense, the hydrogen adsorption value estimated for the $Ni_{0.25}Cu_{0.75}/C$ catalytic surfaces is neither too small nor too large, which maximizes the HER efficiency by optimizing the interactions of the reactants and intermediate species at the electrochemical interfaces. It should be pointed out that the catalytic active sites for hydrogen adsorption were localized at the 3-fold hollow sites of NiCu (111) surfaces (Figure 5).

Our DFT calculations show that $Ni_{0.25}Cu_{0.75}/C$ has a ΔG_{H^*} very close to 0 (−0.05 eV), surpassing by far the values for $Ni_{0.75}Cu_{0.25}/C$ (0.62 eV), $Ni_{0.50}Cu_{0.50}/C$ (0.38 eV), Cu/C (−0.29 eV), and Ni/C (0.86 eV) (Figure 6F). The relationship between the experimentally measured C_{dl} and ΔG_{H^*} values of the five electrocatalysts is shown in Figure 6G. For $Ni_{0.25}Cu_{0.75}/C$, the smallest value of ΔG_{H^*} together with the largest C_{dl} determines the observed optimized HER activity. We have also calculated the hydrogen turn over frequency (TOF) for all of the electrocatalysts to further investigate their intrinsic HER performance. The TOF value for $Ni_{0.25}Cu_{0.75}/C$ is several times higher than for the others studied. The experimental TOFs were found to be 0.62, 0.28, 0.10, 0.061, and 0.056 s^{-1} for $Ni_{0.25}Cu_{0.75}/C$, $Ni_{0.75}Cu_{0.25}/C$, $Ni_{0.50}Cu_{0.50}/C$, Ni/C, and Cu/C at −0.15 V, respectively (Table S4). To gain further insight on the nature of the catalytically active sites of the nanoalloys, the number of hydrogen molecules evolved per second per active site were carefully plotted against the potential for each catalyst and $Ni_{0.25}Cu_{0.75}/C$ electrocatalyst showed better performance than the others (Figure 6H). The higher performance of $Ni_{0.25}Cu_{0.75}/C$ can be directly linked to the pronounced interfacial lattice mismatch of its crystal structure which downshifts the d-band and enhances the interaction with the H reactive intermediates decreasing the ΔG_{H^*} values and promoting overall HER activity. The calculated higher mass activity and specific activity values for $Ni_{0.25}Cu_{0.75}/C$ also shows its superior intrinsic activity toward the HER process (Table S4). Finally, $Ni_{0.25}Cu_{0.75}/C$ showed ultrahigh electrochemical stability in acidic media, maintaining 99% of the initial current applied after 20 000 s and surpassing the Pt/C stability under the same experimental conditions (Figure 6I).

3.4. ORR Activities of Ni, Cu, and Bimetallic NiCu Nanostructures. The ORR activity of the carbon-embedded mono- and bimetallic nanoparticles was evaluated via steady-state linear sweep voltammetry (LSV) in O_2-saturated 0.5 M NaOH solution under static and dynamic conditions (Figure 7). Figure S10 compares the resulting voltammetric curves obtained for O_2-saturated and Ar-saturated solutions, displaying very well-defined ORR cathodic peaks and demonstrating that the oxygen electroreduction processes are taking place at the electrochemical interfaces. Remarkably, $Ni_{0.25}Cu_{0.75}/C$ exhibited a more positive oxygen electroreduction peak at 0.67 V vs RHE than those of the other studied catalysts, indicating better electrocatalytic ORR activity than the others. Figure 7A displays the ORR polarization curves for all the catalysts. $Ni_{0.25}Cu_{0.75}/C$ shows a much higher value of the onset potential (0.95 V vs RHE) and the half-wave potential (0.80 vs RHE) than the other mono- and bimetallic catalysts. The performance is comparable or even better than for many other recently reported ORR electrocatalysts (Table S9). Furthermore, the Tafel plots and the ECSA normalized ORR polarization curves also confirmed the superior ORR activity of $Ni_{0.25}Cu_{0.75}/C$, demonstrating both the larger intrinsic activity and faster kinetics than the other systems (Figure 7B and Figure 7C). In contrast with the observed OER and HER trends, the other two bimetallic catalysts show very similar ORR performance compared with those of the monometallic catalysts (Table S5).

To gain further insights into the kinetic parameters for the ORR, rotating-disk voltammetry (RDV) measurements were performed at different rotation rates, between 250 and 2500 rpm, at a scan rate of 10 $mV{\cdot}s^{-1}$ (Figure 7D). The onset ORR potential was found to be 0.96 V vs RHE. The inset of Figure 7D shows the resulting K−L plot for $Ni_{0.25}Cu_{0.75}/C$. The excellent fit confirms a first-order reaction for dissolved O_2.[57] Using the K−L equations, the average number of electrons transferred (n) per oxygen molecule at 0.6 V vs RHE and the resulting kinetic-limiting current density (J_k) values were estimated to be 4.106 and 10.63 $mA{\cdot}cm^{-2}$, respectively. The number of electrons exchanged per O_2 molecule with $Ni_{0.25}Cu_{0.75}/C$ is close to 4, indicating that the electrochemical reaction follows the most efficient electron pathway. Additionally, the difference of anodic and cathodic current densities as a function of scan rates was plotted for all the samples. As seen in the OER section, $Ni_{0.25}Cu_{0.75}/C$ displays the larger C_{dl} value in the alkaline media and therefore, it possesses the largest number of ORR active sites.

The electrocatalytic performance can be tuned by varying the oxygen binding energy (E_{OB}) which constitutes a good descriptor of the catalytic efficiency of a large portfolio of reactions. Considering the Sabatier rule, very strong binding energies lead to surface oxidation, which decreases the catalytic activity, while very weak binding energies give rise to a fast desorption of the oxygen from the active site. Consequently, optimized ORR activity requires moderate E_{OB} values, balancing both the surface oxidation and desorption processes at the same time. To obtain a better understanding of the superior ORR activity of $Ni_{0.25}Cu_{0.75}/C$, we have plotted the onset potential and unit cell volume values as a function of the DFT-calculated oxygen binding energy values (E_{OB}) (Figure 7E). Among all, $Ni_{0.25}Cu_{0.75}/C$ exhibits an optimum oxygen binding energy for electroreduction which is the midway value

https://dx.doi.org/10.1021/jacs.0c06960
J. Am. Chem. Soc. 2020, 142, 14688−14701

between the oxygen binding energies for the pure metallic nanoparticles. The lowest unit cell volume value of $Ni_{0.25}Cu_{0.75}/C$ reflects that the lattice contraction, and therefore, the high strain energy strongly helps to improve the ORR catalytic rates as well as to reduce the binding energy of oxygen-based adsorbates, such as O* and OH*, thus increasing the electron transfer rates at the catalytically active surface sites.[58,59] Our DFT calculations showed a good agreement with the experimental results. In detail, a significant reduction of the Gibbs free energies for the O*, OH*, and OOH* intermediate catalytic species was observed (Figure 7F). $Ni_{0.25}Cu_{0.75}/C$ exhibited a lower η^{ORR} value (0.87 eV) than those for $Ni_{0.75}Cu_{0.25}/C$ (1.23 eV), $Ni_{0.50}Cu_{0.50}/C$ (0.96 eV), Cu/C (3.52 eV), and Ni/C (1.32 eV) (Figure 7G) as well as the C_{dl} of $Ni_{0.25}Cu_{0.75}/C$ is better than for all catalysts, indicating that the electrochemical performance is optimized for this Ni:Cu ratio. The calculated mass activity and specific activity values for the electrocatalysts are presented in Figure 7H. Like for the OER and HER processes, the TOF, mass activity and specific activity of the electrocatalysts were calculated at 0.75 V vs RHE (Table S5) and it was found that $Ni_{0.25}Cu_{0.75}/C$ exhibits the best intrinsic activity toward the ORR process. Finally, $Ni_{0.25}Cu_{0.75}/C$ showed an excellent long-term electrochemical stability compared to commercial Pt/C, keeping 91% of the initial current applied after 20 000 s (Figure 7I).

4. CONCLUSIONS

In summary, we report the facile synthesis of trifunctional bimetallic NiCu nanoparticles encapsulated in carbon that allows the systematic control of the structure and the electronic properties thus, producing effective catalysts for HER, OER, and ORR reactions. The Ni:Cu ratio was varied to control the structural and electronic properties of the bimetallic nanoparticles. Experimentally and theoretically, it was established that the local distortion of the crystalline lattice at the bimetallic nanostructured surfaces was associated with the downshift of the d-band and the lowering of the binding energies of the intermediate reactive species, which in turn increases the electron transfer rates of the catalytically active surface sites and improves the overall reaction rates. The DFT-calculated binding energy values were used as desirable parameters to describe the trifunctional electrocatalytic efficiency of the bimetallic nanoalloys. Thus, the nanocomposite $Ni_{0.25}Cu_{0.75}/C$, which exhibits a near-optimal binding energy for HER, OER, and ORR reactions, shows an impressive trifunctional catalytic activity that outperforms commercial Pt and RuO_2 catalysts. Our findings provide in-depth insights to directly correlate the structure−catalytic function relationships of carbon-encapsulated NiCu bimetallic nanostructures, thus paving the way toward the rational design of low-cost and scalable multifunctional catalytic nanosystems.

■ ASSOCIATED CONTENT

Supporting Information

The Supporting Information is available free of charge at https://pubs.acs.org/doi/10.1021/jacs.0c06960.

Computational methods; lattice constant calculation; TOF calculation, surface composition of the electrocatalysts obtained by the XPS measurements; comparison of OER, HER, and ORR performance of Cu/C, Ni/C, $Ni_{0.50}Cu_{0.50}/C$, $Ni_{0.75}Cu_{0.25}/C$, and $Ni_{0.25}Cu_{0.75}/C$ electrocatalysts; the obtained C_{dl}, ECSA, and RF values for different electrocatalysts in HER and OER conditions; comparison of OER, HER, and ORR performances of $Ni_{0.25}Cu_{0.75}/C$ with previously reported electrocatalysts; slab model; EDS, TEM, and XPS analysis; LSV and CV measurements (PDF)

■ AUTHOR INFORMATION

Corresponding Authors

Alain R. Puente Santiago − *Department of Chemistry and Biochemistry, University of Texas at El Paso, El Paso, Texas 79968, United States;* orcid.org/0000-0002-8491-3565; Email: arpuentesan@utep.edu

Luis Echegoyen − *Department of Chemistry and Biochemistry, University of Texas at El Paso, El Paso, Texas 79968, United States;* orcid.org/0000-0003-1107-9423; Email: echegoyen@utep.edu

Sreeprasad T. Sreenivasan − *Department of Chemistry and Biochemistry, University of Texas at El Paso, El Paso, Texas 79968, United States;* orcid.org/0000-0002-5728-0512; Email: sreenivasan@utep.edu

Juan C. Noveron − *Department of Chemistry and Biochemistry, University of Texas at El Paso, El Paso, Texas 79968, United States; Nanosystems Engineering Research Center for Nanotechnology-Enabled Water Treatment, Houston, Texas 77005, United States;* orcid.org/0000-0002-2762-7802; Email: jcnoveron@utep.edu

Authors

Md Ariful Ahsan − *Department of Chemistry and Biochemistry, University of Texas at El Paso, El Paso, Texas 79968, United States; Nanosystems Engineering Research Center for Nanotechnology-Enabled Water Treatment, Houston, Texas 77005, United States;* orcid.org/0000-0002-2024-8690

Yu Hong − *Department of Mechanical Engineering, Colorado School of Mines, Golden, Colorado 40801, United States*

Ning Zhang − *Department of Aerospace Engineering and Mechanics, The University of Alabama, Tuscaloosa, Alabama 35487, United States;* orcid.org/0000-0002-4066-1837

Manuel Cano − *Department of Physical Chemistry and Applied Thermodynamics, Institute of Fine Chemistry and Nanochemistry (IUNAN), University of Córdoba, E-14014 Córdoba, Spain;* orcid.org/0000-0002-0810-2920

Enrique Rodriguez-Castellon − *Department of Inorganic Chemistry, Crystallography and Mineralogy, Faculty of Sciences University of Málaga, E-29016 Málaga, Spain;* orcid.org/0000-0003-4751-1767

Complete contact information is available at: https://pubs.acs.org/10.1021/jacs.0c06960

Notes

The authors declare no competing financial interest.

■ ACKNOWLEDGMENTS

This research was funded in part by the US National Science Foundation (NSF) Nanotechnology-Enabled Water Treatment Center (NEWT ERC435 1449500) (to J.C.N.), the USDA 2019-38422-30214 (to J.C.N.), the NSF CHE-18001317 (to L.E.). The Robert A. Welch Foundation is gratefully acknowledged for an endowed chair to L.E. (grant AH-0033), and the Ralph & Kathleen Ponce de Leon Professorship to J.C.N is gratefully acknowledged. We would

also like to thank Dr. Candace Chan and her student J. Mark Weller for the STEM and EELS analysis. SS would like to acknowledge the support through UTEP start-up, UT STARs, URI funding, and NSF-PREM grant #DMR-1827745. E.R.C. gives thanks to project RTI2018-099668-BC22 of Ministerio de Ciencia, Innovación y Universidades and FEDER funds. M.C. thanks the Andalusian Government (Consejería de Economía, Conocimiento, Empresas y Universidades, Junta de Andalucía) from Spain for its financial support through UCO-1263193 project.

REFERENCES

(1) Yuan, K.; Lutzenkirchen-Hecht, D.; Li, L.; Shuai, L.; Li, Y.; Cao, R.; Qiu, M.; Zhuang, X.; Leung, M. K. H.; Chen, Y.; Scherf, U. Boosting Oxygen Reduction of Single Iron Active Sites via Geometric and Electronic Engineering: Nitrogen and Phosphorus Dual-Coordination. *J. Am. Chem. Soc.* **2020**, *142*, 2404−2412.

(2) Tao, H. B.; Zhang, J.; Chen, J.; Zhang, L.; Xu, Y.; Chen, J. G.; Liu, B. Revealing Energetics of Surface Oxygen Redox from Kinetic Fingerprint in Oxygen Electrocatalysis. *J. Am. Chem. Soc.* **2019**, *141* (35), 13803−13811.

(3) Chu, S.; Cui, Y.; Liu, N. The path towards sustainable energy. *Nat. Mater.* **2017**, *16* (1), 16−22.

(4) Stamenkovic, V. R.; Strmcnik, D.; Lopes, P. P.; Markovic, N. M. Energy and fuels from electrochemical interfaces. *Nat. Mater.* **2017**, *16* (1), 57−69.

(5) Tsang, C. H. A.; Huang, H.; Xuan, J.; Wang, H.; Leung, D. Graphene materials in green energy applications: Recent development and future perspective. *Renewable Sustainable Energy Rev.* **2020**, *120*, 109656.

(6) Li, Y.; Guo, S. Noble metal-based 1D and 2D electrocatalytic nanomaterials: Recent progress, challenges and perspectives. *Nano Today* **2019**, *28*, 100774.

(7) Zhu, Y. P.; Guo, C.; Zheng, Y.; Qiao, S.-Z. Surface and interface engineering of noble-metal-free electrocatalysts for efficient energy conversion processes. *Acc. Chem. Res.* **2017**, *50* (4), 915−923.

(8) Gao, R.; Dai, Q.; Du, F.; Yan, D.; Dai, L. C60-Adsorbed Single-Walled Carbon Nanotubes as Metal-Free, pH-Universal, and Multifunctional Catalysts for Oxygen Reduction, Oxygen Evolution, and Hydrogen Evolution. *J. Am. Chem. Soc.* **2019**, *141* (29), 11658−11666.

(9) Liu, X.; Liu, W.; Ko, M.; Park, M.; Kim, M. G.; Oh, P.; Chae, S.; Park, S.; Casimir, A.; Wu, G.; Cho, J. Metal (Ni, Co)-metal oxides/graphene nanocomposites as multifunctional electrocatalysts. *Adv. Funct. Mater.* **2015**, *25* (36), 5799−5808.

(10) Jiang, J.; Liu, Q.; Zeng, C.; Ai, L. Cobalt/molybdenum carbide@ N-doped carbon as a bifunctional electrocatalyst for hydrogen and oxygen evolution reactions. *J. Mater. Chem. A* **2017**, *5* (32), 16929−16935.

(11) Han, N.; Yang, K. R.; Lu, Z.; Li, Y.; Xu, W.; Gao, T.; Cai, Z.; Zhang, Y.; Batista, V. S.; Liu, W.; Sun, X. Nitrogen-doped tungsten carbide nanoarray as an efficient bifunctional electrocatalyst for water splitting in acid. *Nat. Commun.* **2018**, *9* (1), 1−10.

(12) Zou, H.; Li, G.; Duan, L.; Kou, Z.; Wang, J. In situ coupled amorphous cobalt nitride with nitrogen-doped graphene aerogel as a trifunctional electrocatalyst towards Zn-air battery deriven full water splitting. *Appl. Catal., B* **2019**, *259*, 118100.

(13) Wei, C.; Sun, Y.; Scherer, G. G.; Fisher, A. C.; Sherburne, M. P.; Ager, J. W.; Xu, Z. J. Surface Composition Dependent Ligand Effect in Tuning the Activity of Nickel-copper Bimetallic Electrocatalysts towards Hydrogen Evolution in Alkaline. *J. Am. Chem. Soc.* **2020**, *142*, 7765−7775.

(14) Yang, L.; Wang, D.; Lv, Y.; Cao, D. Nitrogen-doped graphitic carbons with encapsulated CoNi bimetallic nanoparticles as bifunctional electrocatalysts for rechargeable Zn−Air batteries. *Carbon* **2019**, *144*, 8−14.

(15) Pi, Y.; Shao, Q.; Wang, P.; Guo, J.; Huang, X. General formation of monodisperse IrM (M= Ni, Co, Fe) bimetallic nanoclusters as bifunctional electrocatalysts for acidic overall water splitting. *Adv. Funct. Mater.* **2017**, *27* (27), 1700886.

(16) Li, C.; Wu, M.; Liu, R. High-performance bifunctional oxygen electrocatalysts for zinc-air batteries over mesoporous Fe/Co-NC nanofibers with embedding FeCo alloy nanoparticles. *Appl. Catal., B* **2019**, *244*, 150−158.

(17) Sha, L.; Yin, J.; Ye, K.; Wang, G.; Zhu, K.; Cheng, K.; Yan, J.; Wang, G.; Cao, D. The construction of self-supported thorny leaf-like nickel-cobalt bimetal phosphides as efficient bifunctional electrocatalysts for urea electrolysis. *J. Mater. Chem. A* **2019**, *7* (15), 9078−9085.

(18) Khalid, M.; Honorato, A. M.; Tremiliosi Filho, G.; Varela, H. Trifunctional catalytic activities of trimetallic FeCoNi alloy nanoparticles embedded in a carbon shell for efficient overall water splitting. *J. Mater. Chem. A* **2020**, *8* (18), 9021−9031.

(19) Pan, Y.; Liu, S.; Sun, K.; Chen, X.; Wang, B.; Wu, K.; Cao, X.; Cheong, W. C.; Shen, R.; Han, A.; et al. A Bimetallic Zn/Fe Polyphthalocyanine-Derived Single-Atom Fe-N4 Catalytic Site: A Superior Trifunctional Catalyst for Overall Water Splitting and Zn−Air Batteries. *Angew. Chem., Int. Ed.* **2018**, *57* (28), 8614−8618.

(20) Islam, Q. A.; Majee, R.; Bhattacharyya, S. Bimetallic nanoparticle decorated perovskite oxide for state-of-the-art trifunctional electrocatalysis. *J. Mater. Chem. A* **2019**, *7* (33), 19453−19464.

(21) Liu, X.; Yang, W.; Chen, L.; Liu, Z.; Long, L.; Wang, S.; Liu, C.; Dong, S.; Jia, J. Graphitic Carbon Nitride (g-C3N4) Derived Bamboo-like Carbon Nanotubes/Co Nanoparticles Hybrids for Highly Efficient Electrocatalytic Oxygen Reduction. *ACS Appl. Mater. Interfaces* **2020**, *12*, 4463−4472.

(22) De Silva, U.; Masud, J.; Zhang, N.; Hong, Y.; Liyanage, W. P.; Zaeem, M. A.; Nath, M. Nickel telluride as a bifunctional electrocatalyst for efficient water splitting in alkaline medium. *J. Mater. Chem. A* **2018**, *6* (17), 7608−7622.

(23) Shit, S.; Chhetri, S.; Jang, W.; Murmu, N. C.; Koo, H.; Samanta, P.; Kuila, T. Cobalt sulfide/nickel sulfide heterostructure directly grown on nickel foam: an efficient and durable electrocatalyst for overall water splitting application. *ACS Appl. Mater. Interfaces* **2018**, *10* (33), 27712−27722.

(24) Luo, S.; Song, H.; Philo, D.; Oshikiri, M.; Kako, T.; Ye, J. Solar-driven production of hydrogen and acetaldehyde from ethanol on Ni-Cu bimetallic catalysts with solar-to-fuels conversion efficiency up to 3.8%. *Appl. Catal., B* **2020**, *272*, 118965.

(25) Chen, Z.; Wu, R.; Liu, Y.; Ha, Y.; Guo, Y.; Sun, D.; Liu, M.; Fang, F. Ultrafine Co nanoparticles encapsulated in carbon-nanotubes-grafted graphene sheets as advanced electrocatalysts for the hydrogen evolution reaction. *Adv. Mater.* **2018**, *30* (30), 1802011.

(26) Qiao, L.; Zhu, A.; Yang, H.; Zeng, W.; Dong, R.; Tan, P.; Zhong, D.; Ma, Q.; Pan, J. Copper−nickel embedded into a nitrogen-doped carbon octahedron as an effective bifunctional electrocatalyst. *Inorg. Chem. Front.* **2018**, *5* (9), 2276−2283.

(27) Ji, D.; Fan, L.; Li, L.; Peng, S.; Yu, D.; Song, J.; Ramakrishna, S.; Guo, S. Atomically Transition Metals on Self-Supported Porous Carbon Flake Arrays as Binder-Free Air Cathode for Wearable Zinc−Air Batteries. *Adv. Mater.* **2019**, *31* (16), 1808267.

(28) Zhang, J.; Sun, Y.; Zhu, J.; Gao, Z.; Li, S.; Mu, S.; Huang, Y. Ultranarrow graphene nanoribbons toward oxygen reduction and evolution reactions. *Adv. Sci.* **2018**, *5* (12), 1801375.

(29) Ding, R.; Chen, Q.; Luo, Q.; Zhou, L.; Wang, Y.; Zhang, Y.; Fan, G. Salt template-assisted in situ construction of Ru nanoclusters and porous carbon: Excellent catalysts toward hydrogen evolution, ammonia-borane hydrolysis, and 4-nitrophenol reduction. *Green Chem.* **2020**, *22*, 835−842.

(30) Su, Y.; Zhu, Y.; Jiang, H.; Shen, J.; Yang, X.; Zou, W.; Chen, J.; Li, C. Cobalt nanoparticles embedded in N-doped carbon as an efficient bifunctional electrocatalyst for oxygen reduction and evolution reactions. *Nanoscale* **2014**, *6* (24), 15080−15089.

(31) Pearson, D.; Ahn, C.; Fultz, B. White lines and d-electron occupancies for the 3d and 4d transition metals. *Phys. Rev. B: Condens. Matter Mater. Phys.* **1993**, *47* (14), 8471.

https://dx.doi.org/10.1021/jacs.0c06960
J. Am. Chem. Soc. 2020, 142, 14688−14701

(32) Mitsuru, W.; Satoshi, M.; Yoshikazu, H.; Katsura, K.; Hiroyuki, U.; Masahiro, W. Electronic structures of PtÀCo and PtÀRu alloys for CO-tolerant anode catalysts in polymer electrolyte fuel cells studied by ECÀXPS. *J. Phys. Chem. B* **2006**, *110*, 23489−23496.
(33) Chu, M.; Chen, C.; Guo, W.; Lu, L.; Wu, Y.; Wu, H.; He, M.; Han, B. Enhancing electroreduction of CO 2 over Bi 2 WO 6 nanosheets by oxygen vacancies. *Green Chem.* **2019**, *21* (10), 2589−2593.
(34) Li, S.; Chen, W.; Pan, H.; Cao, Y.; Jiang, Z.; Tian, X.; Hao, X.; Maiyalagan, T.; Jiang, Z.-J. FeCo alloy nanoparticles coated by an ultrathin N-doped carbon layer and encapsulated in carbon nanotubes as a highly efficient bifunctional air electrode for rechargeable Zn-air batteries. *ACS Sustainable Chem. Eng.* **2019**, *7* (9), 8530−8541.
(35) Zhang, Y.; Ouyang, B.; Xu, J.; Jia, G.; Chen, S.; Rawat, R. S.; Fan, H. J. Rapid synthesis of cobalt nitride nanowires: Highly efficient and low-cost catalysts for oxygen evolution. *Angew. Chem., Int. Ed.* **2016**, *55* (30), 8670−8674.
(36) Anantharaj, S.; Kundu, S. Do the Evaluation Parameters Reflect Intrinsic Activity of Electrocatalysts in Electrochemical Water Splitting? *ACS Energy Lett.* **2019**, *4* (6), 1260−1264.
(37) Smith, R. D.; Pasquini, C.; Loos, S.; Chernev, P.; Klingan, K.; Kubella, P.; Mohammadi, M. R.; González-Flores, D.; Dau, H. Geometric distortions in nickel (oxy) hydroxide electrocatalysts by redox inactive iron ions. *Energy Environ. Sci.* **2018**, *11* (9), 2476−2485.
(38) Zhou, D.; Wang, S.; Jia, Y.; Xiong, X.; Yang, H.; Liu, S.; Tang, J.; Zhang, J.; Liu, D.; Zheng, L.; et al. NiFe hydroxide lattice tensile strain: enhancement of adsorption of oxygenated intermediates for efficient water oxidation catalysis. *Angew. Chem., Int. Ed.* **2019**, *58* (3), 736−740.
(39) Xia, Z.; Guo, S. Strain engineering of metal-based nanomaterials for energy electrocatalysis. *Chem. Soc. Rev.* **2019**, *48* (12), 3265−3278.
(40) Lu, X.; Zhao, C. Electrodeposition of hierarchically structured three-dimensional nickel−iron electrodes for efficient oxygen evolution at high current densities. *Nat. Commun.* **2015**, *6* (1), 1−7.
(41) Ratnayaka, A.; Marra, V.; Branco, T.; Staras, K. Extrasynaptic vesicle recycling in mature hippocampal neurons. *Nat. Commun.* **2011**, *2* (1), 1−11.
(42) Sun, Y.; Zhao, Z.; Wu, S.; Li, W.; Wu, B.; Liu, G.; Chen, G.; Xu, B.; Kang, B.; Li, Y.; Li, C. D-band Centers Engineering of Perovskite Cobaltite for Enhanced Electrocatalytic Oxygen Evolution. *ChemSusChem* **2020**, *13*, 2671−2676.
(43) He, C.; Huang, M.; Wang, G.; Zhang, Y.; Li, X.; Fan, L.; Li, Y. Synergistic tuning of oxygen vacancies and d-band centers of ultrathin cobaltous dihydroxycarbonate nanowires for enhanced electrocatalytic oxygen evolution. *Nanoscale* **2020**, *12*, 11735.
(44) Lukowski, M. A.; Daniel, A. S.; Meng, F.; Forticaux, A.; Li, L.; Jin, S. Enhanced hydrogen evolution catalysis from chemically exfoliated. *J. Am. Chem. Soc.* **2013**, *135*, 10274.
(45) Zhang, Y.; Ouyang, B.; Xu, J.; Chen, S.; Rawat, R. S.; Fan, H. J. 3D porous hierarchical nickel−molybdenum nitrides synthesized by RF plasma as highly active and stable hydrogen-evolution-reaction electrocatalysts. *Adv. Energy Mater.* **2016**, *6* (11), 1600221.
(46) Chen, W. F.; Sasaki, K.; Ma, C.; Frenkel, A. I.; Marinkovic, N.; Muckerman, J. T.; Zhu, Y.; Adzic, R. R. Hydrogen-evolution catalysts based on non-noble metal nickel−molybdenum nitride nanosheets. *Angew. Chem., Int. Ed.* **2012**, *51* (25), 6131−6135.
(47) Hu, M.; Linder, D. P.; Buongiorno Nardelli, M.; Striolo, A. Hydrogen adsorption on platinum−gold bimetallic nanoparticles: A density functional theory study. *J. Phys. Chem. C* **2013**, *117* (29), 15050−15060.
(48) Choi, S.; Lee, S.; Kim, W.; Choi, R.; Hong, K.; Nam, K.; Han, S.; Park, J. *ACS Appl. Mater. Interfaces* **2012**, *4*, 6228.
(49) Cui, C.-H.; Yu, J.-W.; Li, H.-H.; Gao, M.-R.; Liang, H.-W.; Yu, S.-H. Remarkable enhancement of electrocatalytic activity by tuning the interface of Pd−Au bimetallic nanoparticle tubes. *ACS Nano* **2011**, *5* (5), 4211−4218.
(50) Luo, M.; Guo, S. Strain-controlled electrocatalysis on multimetallic nanomaterials. *Nat. Rev. Mater.* **2017**, *2* (11), 1−13.
(51) Wang, X.; Zhu, Y.; Vasileff, A.; Jiao, Y.; Chen, S.; Song, L.; Zheng, B.; Zheng, Y.; Qiao, S.-Z. Strain effect in bimetallic electrocatalysts in the hydrogen evolution reaction. *ACS Energy Lett.* **2018**, *3* (5), 1198−1204.
(52) Sneed, B. T.; Young, A. P.; Tsung, C.-K. Building up strain in colloidal metal nanoparticle catalysts. *Nanoscale* **2015**, *7* (29), 12248−12265.
(53) Korte, C.; Peters, A.; Janek, J.; Hesse, D.; Zakharov, N. Ionic conductivity and activation energy for oxygen ion transport in superlattices—the semicoherent multilayer system. *Phys. Chem. Chem. Phys.* **2008**, *10* (31), 4623−4635.
(54) Ren, W.; Zang, W.; Zhang, H.; Bian, J.; Chen, Z.; Guan, C.; Cheng, C. PtCo bimetallic nanoparticles encapsulated in N-doped carbon nanorod arrays for efficient electrocatalysis. *Carbon* **2019**, *142*, 206−216.
(55) Alinezhad, A.; Gloag, L.; Benedetti, T. M.; Cheong, S.; Webster, R. F.; Roelsgaard, M.; Iversen, B. B.; Schuhmann, W.; Gooding, J. J.; Tilley, R. D. Direct growth of highly strained Pt islands on branched Ni nanoparticles for improved hydrogen evolution reaction activity. *J. Am. Chem. Soc.* **2019**, *141* (41), 16202−16207.
(56) Wu, J.; Li, P.; Pan, Y.-T. F.; Warren, S.; Yin, X.; Yang, H. Surface lattice-engineered bimetallic nanoparticles and their catalytic properties. *Chem. Soc. Rev.* **2012**, *41* (24), 8066−8074.
(57) Tuci, G.; Zafferoni, C.; Rossin, A.; Milella, A.; Luconi, L.; Innocenti, M.; Truong Phuoc, L.; Duong-Viet, C.; Pham-Huu, C.; Giambastiani, G. Chemically functionalized carbon nanotubes with pyridine groups as easily tunable N-decorated nanomaterials for the oxygen reduction reaction in alkaline medium. *Chem. Mater.* **2014**, *26* (11), 3460−3470.
(58) Zhao, Y.; Wu, Y.; Liu, J.; Wang, F. Dependent Relationship between Quantitative Lattice Contraction and Enhanced Oxygen Reduction Activity over Pt−Cu Alloy Catalysts. *ACS Appl. Mater. Interfaces* **2017**, *9* (41), 35740−35748.
(59) Ma, Z.; Cano, Z. P.; Yu, A.; Chen, Z.; Jiang, G.; Fu, X.; Yang, L.; Wu, T.; Bai, Z.; Lu, J. Enhancing Oxygen Reduction Activity of Pt-based Electrocatalysts: from Theoretical Mechanisms to Practical Methods. *Angew. Chem., Int. Ed.* **2020**, DOI: 10.1002/anie.202003654.

https://dx.doi.org/10.1021/jacs.0c06960
J. Am. Chem. Soc. 2020, 142, 14688−14701